


Research Paper

HIPPI-2: A versatile high-precision polarimeter

Jeremy Bailey¹ , Daniel V. Cotton^{1,2,3}, Lucyna Kedziora-Chudczer^{1,3}, Ain De Horta² and Darren Maybour²

¹School of Physics, UNSW Sydney, New South Wales, 2052, Australia, ²Western Sydney University, Locked Bag 1797, Penrith-South DC, NSW 1797, Australia and

³Centre for Astrophysics, University of Southern Queensland, Toowoomba, Queensland, 4350, Australia

Abstract

We describe the High-Precision Polarimetric Instrument-2 (HIPPI-2) a highly versatile stellar polarimeter developed at the University of New South Wales. Two copies of HIPPI-2 have been built and used on the 60-cm telescope at Western Sydney University's (WSU) Penrith Observatory, the 8.1-m Gemini North Telescope at Mauna Kea and extensively on the 3.9-m Anglo-Australian Telescope (AAT). The precision of polarimetry, measured from repeat observations of bright stars in the SDSS g' band, is better than 3.5 ppm (parts per million) on the 3.9-m AAT and better than 11 ppm on the 60-cm WSU telescope. The precision is better at redder wavelengths and poorer in the blue. On the Gemini North 8-m telescope, the performance is limited by a very large and strongly wavelength-dependent TP that reached 1000's of ppm at blue wavelengths and is much larger than we have seen on any other telescope.

Keywords: instrumentation: polarimeters—polarisation—techniques: polarimetric

(Received 5 August 2019; revised 27 September 2019; accepted 06 November 2019)

1. Introduction

Polarisation measurements of stars using ground-based telescopes can be made with very high levels of precision. As a differential measurement, polarimetry is not subject to the same atmospheric effects that limit the precision of photometry. Techniques based on rapid modulation using photoelastic modulator technology (Kemp & Barbour 1981) have enabled the development of stellar polarimeters capable of parts per million (PPM) levels of precision (Hough et al. 2006; Wiktorowicz & Matthews 2008; Wiktorowicz & Nofi 2015). High precisions (~ 10 ppm) have also been achieved using a double-image polarimeter with a rotating waveplate modulator (Piirola et al. 2014).

The High-Precision Polarimetric Instrument (HIPPI, Bailey et al. 2015) used an alternate approach based on a ferroelectric liquid crystal (FLC) modulator. HIPPI was used on the 3.9-m Anglo-Australian Telescope (AAT), was commissioned in 2014, and demonstrated a precision on bright stars of 4.3 ppm in fractional polarisation (Bailey et al. 2015). HIPPI has been successfully used for a range of science programmes including surveys of polarisation in bright stars (Cotton et al. 2016a), the first detection of polarisation due to rotational distortion in hot stars (Cotton et al. 2017a), studies of the polarisation in active dwarfs (Cotton et al. 2017b, 2019a), the interstellar medium (Cotton et al. 2017b, 2019b), and hot dust (Marshall et al. 2016), and some of the most sensitive searches for polarised reflected light from exoplanets (Bott et al. 2016, 2018).

HIPPI-2 is a redesigned instrument that incorporates a number of improvements based on our experience with—and extensive use of—HIPPI, as well as with the compact and lightweight

Mini-HIPPI instrument (Bailey et al. 2017). HIPPI-2 shares with its predecessors the use of FLC modulators, a polarising beam splitter prism, and photomultiplier tubes (PMTs) as detectors. However, HIPPI-2 uses a redesigned optical system, a new, largely 3D printed, construction, and a compact low-power electronics system that replaces ~ 30 kg of rack-mount electronics in the original HIPPI, with a single compact electronics box weighing 1.3 kg. HIPPI-2 provides improvements in optical throughput and observing efficiency. It is sufficiently compact and lightweight to be easily mounted on small telescopes such as the Western Sydney University (WSU) 60-cm telescope, but powerful enough to provide unique capabilities to very large telescopes.

In this paper, we describe the HIPPI-2 instrument and its data reduction and analysis techniques, and evaluate its performance using observations on three telescopes: the 60-cm Ritchey–Chrétien telescope at WSU's Penrith Observatory, the 3.9-m AAT at Siding Spring Observatory, New South Wales, and the 8.1-m Gemini North telescope at Mauna Kea, Hawaii.

2. Instrument description

2.1. Overview

The optical system of HIPPI-2 is shown in Figure 1 which is adapted from the similar figure for HIPPI in Bailey et al. (2015). HIPPI-2 is designed for a slower input beam ($f/16$) rather than the $f/8$ used in HIPPI. This allows the instrument to dispense with the collimating lenses used in HIPPI. The same Fabry lenses (Thorlabs AC127-019A) and Wollaston prism (Thorlabs WP10-A) used in HIPPI are used for HIPPI-2. The rotating section of the instrument is now the whole instrument, rather than just the prism and detectors as in HIPPI.

The Gemini North telescope has an $f/16$ focal ratio that matches HIPPI-2. On the AAT, it was intended to use HIPPI-2

Author for correspondence: Jeremy Bailey, E-mail: j.bailey@unsw.edu.au

Cite this article: Bailey J, Cotton DV, Kedziora-Chudczer L, De Horta A and Maybour D. (2020) HIPPI-2: A versatile high-precision polarimeter. *Publications of the Astronomical Society of Australia* 37, e004, 1–20. <https://doi.org/10.1017/pasa.2019.45>

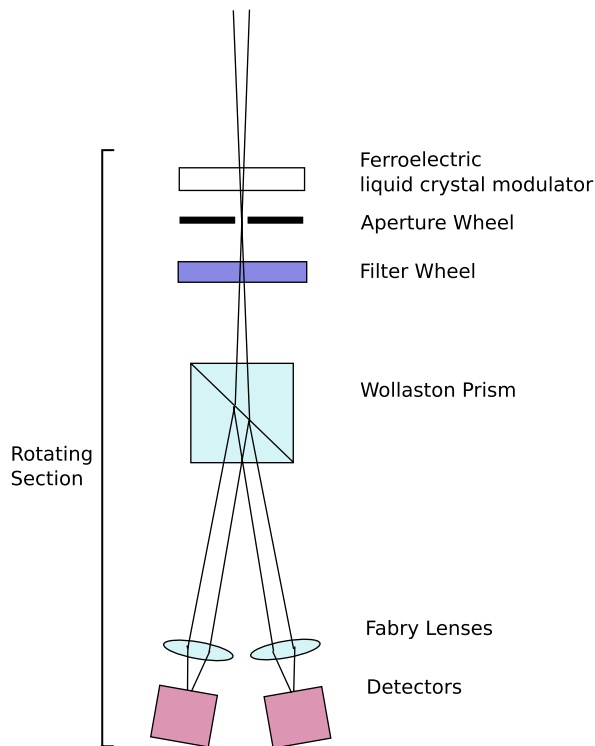


Figure 1. Schematic diagram of HIPPI-2 optical system (not to scale).

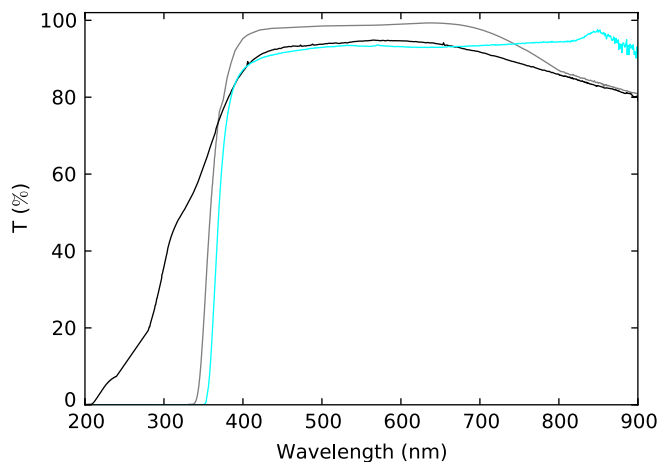


Figure 2. The transmission of HIPPI-2 optical components: Wollaston prism (black), Fabry lens (grey), negative achromatic lens (cyan). The transmission data were generated using a combination of manufacturer data and data acquired with a Cary 1E UV-Vis spectrometer.

at the $f/15$ Cassegrain focus. However, due to problems with the coating of the $f/15$ secondary, it has sometimes been used at the $f/8$ focus, with a -150 -mm focal length negative achromatic lens (Edmund Optics 45423) to convert the beam to approximately $f/16$. On the 60-cm WSU telescope which has an $f/10.5$ focal ratio, the negative lens is also used giving an effective $f/21$ beam.

When used, the transmission of the negative lens sets the short wavelength limit of the instrument response, a role otherwise taken by the Fabry lenses, as shown in Figure 2^a.

^aThe transmission data in Figures 2, 3, and 4 are available in a public repository at github.com/jbaileyAstro/hippi2. The curve representing the transmission of the

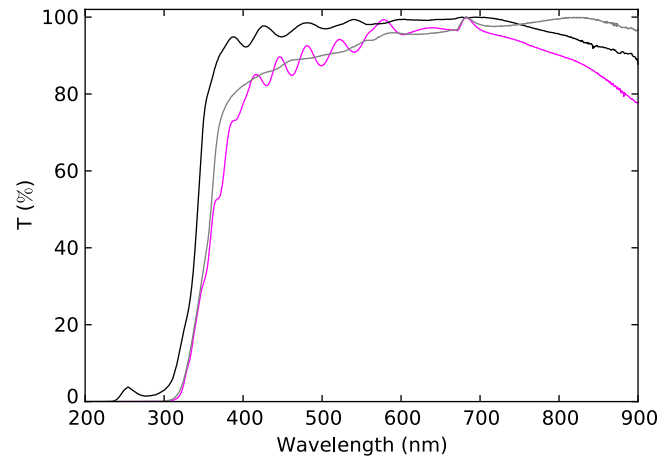


Figure 3. The transmission of FLC modulators used with HIPPI-2: ML (black), BNS (grey); and the Micron Technologies (MT, magenta) unit used with HIPPI and Mini-HIPPI. The transmission data were generated using a Cary 1E UV-Vis spectrometer.

To minimise telescope polarisation (TP) due to inclined mirrors, HIPPI-2 needs to be mounted at a direct Cassegrain focus. On Gemini North, it mounts on the uplooking science port of the Instrument Support Structure to avoid the need to use the science fold mirror. On the AAT, HIPPI-2 mounts on the CURE Cassegrain interface unit (Horton et al. 2012).

2.2. FLC modulators

HIPPI-2 uses FLC modulators operating at 500 Hz for the primary polarisation modulation. FLCs are electrically switched half-wave plates. They have a fixed retardation but the orientation of the fast axis can be switched by applying a square wave voltage.

Two different modulators have been used with HIPPI-2. For the 2018 AAT and WSU telescope observations, we used the same MS Series polarisation rotator from Boulder Nonlinear Systems (BNS), that we previously used with HIPPI. This modulator is driven by a ± 5 V square wave signal. The modulation efficiency of the BNS modulator was described by Bailey et al. (2015). However, we have found its performance to drift over time requiring re-calibration as described later in Section 4.2.1.

For the Gemini North observations and the 2019 observations with the AAT and WSU telescope, we used a 25-mm diameter modulator from Meadowlark Optics (ML) with a design wavelength of 500 nm. This modulator uses a ± 9 V square wave drive signal. We can compare the different modulators using the product of their modulation efficiency and transmission over the wavelength range of interest. The modulation efficiency curves are described in Section 4.2.1, and the transmission of the modulators is shown in Figure 3.

The FLCs are temperature-sensitive devices and so are mounted in temperature-controlled enclosures and operated at a temperature of 25 ± 0.2 °C.

2.3. Filter and aperture wheels

HIPPI-2 includes filter and aperture wheels. HIPPI had a six-position filter wheel and only a single fixed aperture. The provision of an aperture wheel with various size apertures allows the choice

Wollaston prism is one measured using a Cary 1E UV-Vis spectrometer for a similarly coated Thorlabs Glan Taylor prism.

Table 1. HIPPI-2 apertures

Position	Size (mm)	Gemini (arcsec)	AAT (arcsec)	WSU (arcsec)
1	1.6	2.6	5.7	26.2
2	2.6	4.2	9.3	42.6
3	3.6	5.8	12.8	58.9
4	4.75	7.6	16.9	77.8
5	5.65	9.1	20.1	92.5
6	7.7	12.4	27.4	126.0

Table 2. HIPPI-2 filters

Position	Name	λ (nm)	Notes
1 ^a	650LP	>650	Longpass filter
	U	337–392	Omega optics Bessell
2	V	480–590	Omega optics Bessell
3	Clear		No filter
4	r'	562–695	Astrodon Gen 2
5	500SP	<500	Shortpass filter
6	425SP	<425	Shortpass filter
7	Blank		
8	g'	401–550	Astrodon Gen 2

^a Two filters have been used in position 1.

of aperture to be optimised for the seeing conditions and background level and provides a capability to study extended objects such as debris discs and solar system planets. Table 1 lists the standard set of six apertures with the size in arc seconds for Gemini North, the AAT ($f/15$), and WSU 60-cm ($f/21$).

The HIPPI-2 filter wheel has eight positions and can accept 25- or 27-mm diameter circular filters. The set of filters used so far are listed in Table 2. The Blank position in the filter wheel allows measurements of the dark current of the detectors. The SDSS g' and r' filters used in HIPPI-2 are generation 2 filters from Astrodon Photometrics and have substantially higher peak transmission and squarer responses than the filters used in HIPPI. The transmission profile of each filter is shown in Figure 4. It can be seen that the two shortpass filters cut-off at around 300 nm and also have some transmission at wavelengths greater than 650 nm. We use two different detectors with HIPPI-2 (described in the next section), for the one with the bluer response, the longer wavelength leaks are inconsequential.

2.4. Detectors

Following the filter and aperture wheels, the Wollaston prism acts as the polarisation analyser and splits the light into two beams with a 20° separation. A pupil image from each beam is then focused onto the detectors by the achromatic doublet Fabry lenses.

The detectors are compact PMT modules containing a metal-packaged PMT and an integrated high-tension (HT) supply. Depending on the application, HIPPI-2 can be configured with either blue-sensitive or red-sensitive PMTs. The blue-sensitive PMTs (which we denote B) are Hamamatsu H10720-210 modules which have ultra bialkali photocathodes (Nakamura et al. 2010) providing a quantum efficiency of 43% at 400 nm. The red-sensitive PMTs (denoted R) are Hamamatsu H10720-20 modules with extended red multialkali photocathodes. These have

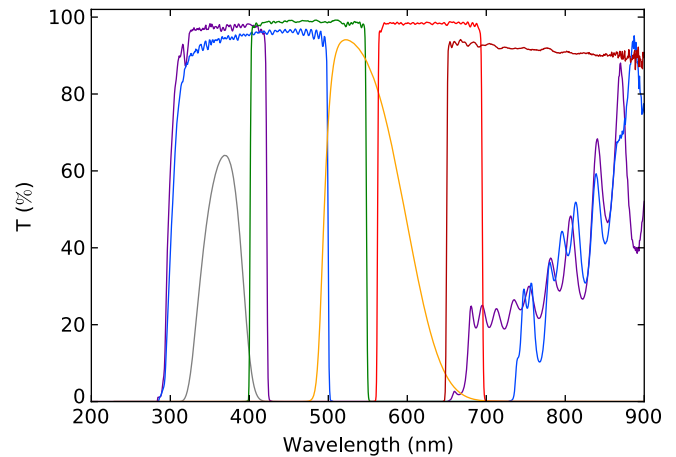


Figure 4. The transmission of the HIPPI-2 filters: U (grey), 425SP (violet), 500SP (blue), g' (green), V (orange), r' (red) and 650LP (brown). The U and V band data are manufacturer data, and the transmission of the other filters has been determined using a Cary 1E UV-Vis spectrometer.

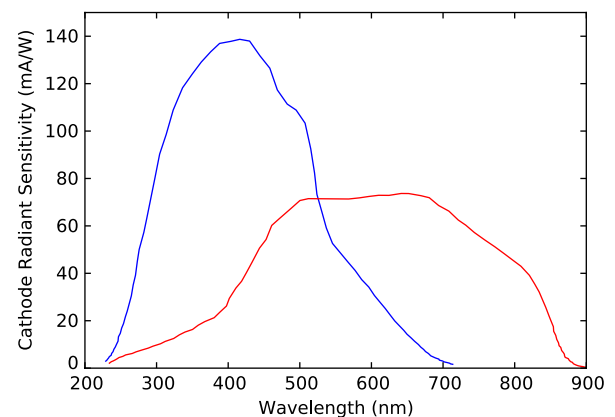


Figure 5. The response of the Hamamatsu H10720-210 (blue) and H10720-20 (red) PMTs in mA/W as provided by the manufacturer. Where needed for bandpass calculations, the data are interpolated to zero outside of the range of the manufacturer data.

a peak quantum efficiency of 19% at 500 nm and response extending to 900 nm. Figure 5 shows the detector response. Switching between blue and red configurations takes 5–10 min.

The detector modules are fitted with a transimpedance amplifier to measure the detector current as described in Bailey et al. (2015). Both the HT supply voltage and transimpedance gain are remotely switchable, and enable a very high dynamic range. On the AAT, HIPPI-2 (like HIPPI) can observe even the brightest stars in the sky while providing close to photon noise limited performance. This ability has proved invaluable in enabling precise calibration and scientific studies of polarisation in bright stars (e.g. Cotton et al. 2017a; Bailey et al. 2019).

2.5. Mechanical construction

HIPPI-2 is designed such that the whole instrument can be rotated around the optical axis. The rotation is performed by a Thorlabs NR360S NanoRotator stage. Apart from this rotator and the optical elements already described, the construction of HIPPI-2 is largely by 3D printing. Most of the optical support structure and optical mounts including the filter and aperture wheels were

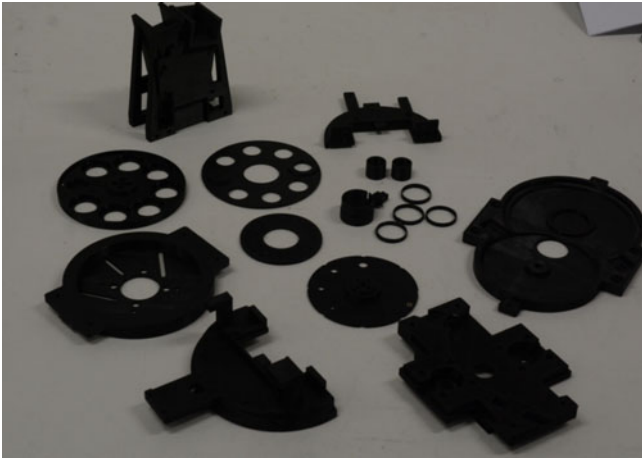


Figure 6. 3D-printed parts for HIPPI-2.

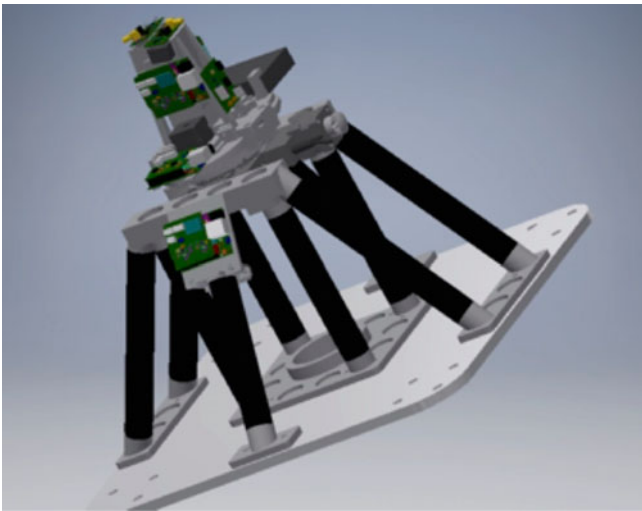


Figure 7. HIPPI-2 on its Gemini North Mounting Frame (CAD drawing). Baffling around the optical path is not shown.

printed in Z-Ultrat material (an enhanced ABS-based plastic) on a Zortrax M200 3D printer (see [Figure 6](#)). Parts for the electronics box were also printed on the same printer. While ABS has a thermal expansion coefficient about three times higher than aluminium, the compact design and slow ($f/16$) optical system mean that the mounting tolerances are not tight and this construction method does not compromise performance.

HIPPI-2 requires a customised mounting for each telescope it is used on. On Gemini North, it has to be supported with its aperture 30 cm below the mounting flange at the telescope science port. This is achieved using an aluminium mounting plate, and a support framework of carbon fibre tubing as shown in [Figure 7](#), which provides a very strong and stiff structure. The carbon fibre tubes and other components are linked by 3D-printed interface pieces (printed on commercial printers in nylon or solid ABS-M30) that are bonded by epoxy to the tubes and bolt to the mounting plate and instrument.

On the AAT, the interface to the CURE mounting flange is made from ABS-M30 plastic and manufactured on a Stratasys industrial grade 3D printer. The mounting for the WSU 60-cm

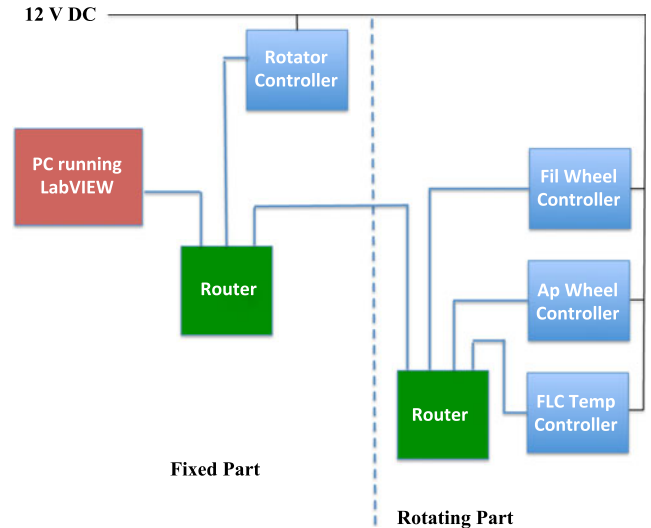


Figure 8. HIPPI-2 control architecture showing the Ethernet links between systems. Only a single power cable and one Ethernet cable run between the fixed and rotating parts of the instrument.

telescope uses a mix of 3D-printed components and carbon fibre tubing.

The only component of HIPPI-2 that required manufacture in a conventional workshop was the aluminium mounting plate for Gemini North. The extensive use of 3D printing, whether on our own printer, or using commercial 3D printing services provides a very fast turnaround that makes possible a rapid prototyping approach to project development. This helps to reduce costs and speeds up development.

2.6. Control electronics and software

The control architecture used for HIPPI-2 is based on hardware and techniques developed for the so-called Internet of Things. Each mechanism or subsystem to be controlled has its own microcontroller which runs a web server and has its own website that can be used to control and interact with the system. In HIPPI-2, for security reasons, the network is a private network rather than the public Internet.

The microcontroller systems used in HIPPI-2 are EtherTen boards from Australian company Freetronics which use an ATmega 328P CPU and include an Ethernet interface. They are programmed in C++ using the Arduino programming interface. We also experimented with a wireless networked system based on ESP8266 processor boards. While the wireless approach worked well, the radio-quiet requirements of the Mauna Kea site led us to adopt the Ethernet-based system.

HIPPI-2 has four subsystems that each have their own microcontroller and web interface. These are the filter and aperture wheels and the FLC temperature controller (these three are all on the rotating part of the instrument) and the instrument rotator (on the fixed part of the instrument). The microcontroller boards and interface electronics are very compact and are mounted on the instrument close to the systems being controlled.

Ethernet routers (Ubiquiti ER-X with five ports) are mounted on both the fixed and rotating parts of the instrument, and allow the architecture shown in [Figure 8](#) with only a single Ethernet cable running between the fixed and rotating parts of

the instrument. We use a special highly flexible cable (Cicoil DC-500-CA003) for this purpose.

A single 12 V DC power supply provides power to all the microcontroller systems as well as the two routers. On board DC-DC converters generate the 5 V needed for the microcontroller and any other required voltages. Three of the microcontroller systems (the rotator and filter and aperture wheel controllers) use essentially identical hardware based on a stepper motor driver. The FLC temperature controller implements a proportional integral (PI) servo to control the drive voltage to a heater, based on feedback from a thermistor temperature sensor.

The microcontroller systems are quite simple devices with relatively slow 8-bit CPUs and lacking an operating system or file system. However, they are small and cheap enough, that we can use one CPU for each mechanism. We do not therefore require them to run complex multitasking or real-time software such as is often used at major observatories where a single CPU controls all the functions in an instrument. The software on each microcontroller is about 300–400 lines of fairly straightforward code. Much of the code can be reused between the different controllers. The only user interface required is a web browser. The hardware and software costs of this approach are very low, and these systems have proved very reliable in operation.

2.7. Data acquisition

The data acquisition system for HIPPI-2 is essentially the same as that used for Mini-HIPPI and described by Bailey et al. (2017). Two National Instruments USB-6211 data acquisition modules are used to read the data from the detectors as well as providing the drive signal for the FLC modulator and controlling the PMT gain and HT voltage. These modules interface via USB to an Intel NUC miniature PC running Windows 10. This computer also provides the interface to the microcontroller systems as shown in Figure 8. The instrument software is adapted from that used for HIPPI and Mini-HIPPI and is written in the LabVIEW graphical programming environment.

The detector signals are read at a 10- μ s sample time, synchronised with the FLC modulation. The data are folded over the modulation period (2 ms for the standard 500 Hz modulation frequency) and written to output files after an integration time of 1–2 s.

2.8. Summary

HIPPI-2 is a compact and low-cost instrument. On its AAT or WSU mounts, the total weight of the instrument is about 4 kg. A compact electronics box weighing 1.3 kg holds the NI interface modules, the computer and the FLC drive electronics and trigger circuitry. The total power requirement for the instrument is about 30 W. The component cost of a complete HIPPI-2 including one set of detectors and filters is about A\$20 000, similar to that of HIPPI, and a little more than that of Mini-HIPPI.

3. Observing procedure

As with Mini-HIPPI, an observation consists of four target measurements at different instrument position angles (PAs): 0°, 45°, 90°, and 135°. Typically, a single-sky measurement (with a shorter exposure time) is made at each PA with the same instrument settings. In changeable conditions or on faint targets, we sometimes bracket each target measurement between two sky

measurements. For bright or highly polarised targets observed in moonless conditions, a single dark measurement can be substituted. Measurements made at the redundant angles (90° and 135°) are combined with the 0° and 45° measurements, respectively, to enable cancellation of instrumental effects. Instrumental polarisation varies with the target's magnitude, the detector voltage settings, and target alignment, so this is an important procedure for obtaining best precision.

HIPPI used the AAT's Cassegrain rotator to rotate the instrument to the four different PAs. With HIPPI-2, the instrument's built-in rotator is used, significantly speeding up observing. HIPPI-2 has two stages of modulation: the electrically driven FLC modulator and the instrument rotation, whereas HIPPI had three stages of modulation, with the third being an instrument back-end rotation swapping the detectors between A and B positions 90° apart. We determined from analysis of HIPPI data that this third stage of modulation provided no significant benefit, allowing the simpler system used in HIPPI-2. Eliminating the back-end rotation and using the instrument rather than the telescope rotator—which reduces the number of target acquisitions from 4 to 1—saves on average 5 min per observation on the AAT.

4. Data reduction and calibration

For data taken on an equatorially mounted telescope, the data processing is a two-step process, involving first a raw data reduction and then correction. Originally, with HIPPI, the first step was performed by a code written in FORTRAN 77, and the second step using a Microsoft EXCEL spreadsheet. Now both steps are performed using programmes written in PYTHON 2.7.5 using elements from the associated packages NUMPY (Oliphant 2006), SCIPY (Jones et al. 2001), MATPLOTLIB (Hunter 2007), ASTROPY (Astropy Collaboration et al. 2013, 2018), ASTROPLAN (Morris et al. 2018), and ASTROQUERY (Ginsburg et al. 2019). Although the mathematics of the process is essentially unchanged, rewriting the software has facilitated some improvements of process and enabled better integration between the steps.

4.1. Raw data reduction

The raw data reduction has three stages: dark and/or sky subtraction; the application of a Mueller matrix model to determine I , Q , and U for each measurement; and combining the measurements for PA 0°, 45°, 90°, and 135° to produce the raw observation.

4.1.1. Dark/Sky subtraction

At each PA, a sky measurement typically consists of 40 one-second integrations. At 500 Hz operation, each integration is made up of 200 modulation points. For each modulation point, an average is calculated from all the integrations, and the resulting average integration subtracted from the target measurement point by point. A dark subtraction uses the same procedure. Lab-based dark measurements made for each detector HT voltage and gain setting are subtracted from each target and sky measurement by default; this is not really necessary when a sky subtraction is applied, but is useful as a monitor of the sky conditions.

4.1.2. Mueller matrix model

Mathematically, the reduction procedure for HIPPI-2 is identical to that of HIPPI as described by Bailey et al. (2015). We can

describe the instrument by a 4-by-4 Mueller matrix \mathbf{M} that relates the output Stokes vector \mathbf{s}_{out} to the input Stokes vector \mathbf{s}_{in} through:

$$\mathbf{s}_{\text{out}} = \mathbf{M}\mathbf{s}_{\text{in}} \quad (1)$$

The Mueller matrix for the instrument is simply the product of the Mueller matrices for its optical components as described by Bailey et al. (2015). The Mueller matrix \mathbf{M} is not a constant but varies through the modulation cycle as the modulator properties change.

We can also define a system matrix \mathbf{W} . The system matrix is an N by 4 matrix, where each row is a state of the system, corresponding to a single data point in the modulation curve. Multiplying the input Stokes vector by the system matrix gives the vector \mathbf{x} of N observed intensities seen at the detector during the modulation cycle (where $N = 200$ is the number of data points in our 500 Hz modulation cycle). It can be seen that each of the N rows of \mathbf{W} is the top row of the Mueller matrix corresponding to that state of the instrument:

$$\mathbf{x} = \mathbf{W}\mathbf{s}_{\text{in}}. \quad (2)$$

The system matrix depends on how the waveplate angle and depolarisation of the modulator vary through the modulation cycle and we determine this through a laboratory calibration procedure in which we feed polarised light of known polarisation states (using a lamp and polariser) into the instrument for a full rotation of the polariser in 10° to 20° steps.

We can then invert equation 2 to give

$$\mathbf{s}_{\text{in}} = \mathbf{W}^+ \mathbf{x}, \quad (3)$$

where \mathbf{W}^+ is the pseudo-inverse of \mathbf{W} , which is calculated numerically. This gives the source Stokes parameters \mathbf{s}_{in} in terms of the observed modulation data \mathbf{x} .

Further details of the procedure can be found in Bailey et al. (2015).

4.1.3. Combining measurements to produce an observation

The final Stokes parameters for an observation are determined by combining the measurements for the four instrument PAs. This step has the effect of cancelling out instrumental polarisation effects. Only the on-axis Stokes parameter determinations are used, so 0° and 90° contribute to Q_i/I , and 45° and 135° to U_i/I . The average of all four measurements contribute to a determination of the I Stokes parameter.

4.2. Correction

The correction step involves three processes: the application of a bandpass model, described in Section 4.2.1, to scale the polarisation magnitude to account for the modulation efficiency of the instrument; a rotation of the co-ordinate frame based on observations of high-polarisation standards; and subtraction of an offset in $q = Q/I$ and $u = U/I$ associated with the TP—determined by observations of low-polarisation standards.

4.2.1. Bandpass model and modulator calibration

A bandpass model is used to make an efficiency correction and determine the effective wavelength of each observation. The bandpass model used for HIPPI-2 is based on that of HIPPI (Bailey et al. 2015), and PlanetPol (Hough et al. 2006) before it, but has been rewritten in PYTHON 2 and is extremely versatile. The same code may be used for any combination of source, atmosphere,

photosensor, modulator, and transmitting (or reflecting) optical components. The bandpass model is integrated into the data processing pipeline, but can also be run independently from the command line or called as a routine in other code enabling full bandpass fitting for science or calibration purposes (e.g. Cotton et al. 2019b).

The effective wavelength is calculated by the bandpass model as

$$\lambda_{\text{eff}} = \frac{\int \lambda S(\lambda) d\lambda}{\int S(\lambda) d\lambda}, \quad (4)$$

where λ is the wavelength and $S(\lambda)$ is the relative contribution to the output detector signal as a function of wavelength. In basic terms, $S(\lambda)$ includes the product of the photocathode radiant sensitivity (in mA/W) and the source spectral energy distribution (SED) as attenuated by functions describing the atmosphere and optical components of the instrument and telescope. Typically,

$$S(\lambda) = F_* T_{\text{atm}} R_{pM} R_{sM} T_{\text{fil}} T_{\text{mod}} T_{\text{anal}} T_{\text{opt}} \mathbb{R}_{ph}, \quad (5)$$

where every term is a function of λ and F_* is the source flux, sometimes modified by reddening, T_{atm} the atmospheric transmission, R_{pM} and R_{sM} the reflectance of the primary and secondary telescope mirrors, T_{fil} , T_{mod} , T_{anal} , and T_{opt} are the transmittance of the filter, modulator, analyser (Wollaston prism), and other optical components in the instrument, respectively, and \mathbb{R}_{ph} the radiant sensitivity of the photosensor.

By default, a Castelli & Kurucz (2004) stellar atmosphere model is used for the SED and sets the resolution of wavelength sampling^b. Included in the bandpass model's standard library are atmosphere models for dwarfs of spectral type O3, B0, A0, F0, G0, K0, M0, and M5^c. For intermediate spectral types, two bandpass models are calculated and the results linearly interpolated in subtype; the same models are used for other spectral classes. The data reduction software uses a look-up file to determine the spectral type of the target, if absent from the file the object's details are downloaded from SIMBAD by the software for stellar objects (using astroquery, Ginsburg et al. 2019) or a solar spectral type assumed for solar system objects. For distant targets, the model SED can be modified to account for interstellar extinction (reddening) using the empirical model of Cardelli et al. (1989). However, most of the targets observed with HIPPI-2 are nearby and by default no reddening is applied.

The Earth atmosphere transmission is based on radiative transfer models pre-calculated using Versatile Software for Transfer of Atmospheric Radiation (VSTAR), (Bailey & Kedziora-Chudczer 2012). Like the optical component data, the spectrum is spline interpolated onto the wavelength grid set by the source. For the observing sites used in this work, standard built-in models were used. The SSO and MK built-in models were used for the AAT and Gemini North observations respectively. For WSU, the built-in mid-latitude summer model adjusted for the altitude of the observatory was used. The transmission is calculated for the airmass at the mid-time of each observation.

The PMT sensitivity (in mA/W) is taken from Hamamatsu data sheets as shown in Figure 5.

In the HIPPI bandpass model, the instrumental transmission was determined as a whole. Lab-based measurements were made with narrowband (NB) filters to estimate the attenuation at blue wavelengths. That procedure lacked precision, and for HIPPI-2 we

^bOptionally, the wavelength grid can be changed, in which case the SED is interpolated onto the desired grid.

^c F_λ units ($\text{erg s}^{-1} \text{cm}^{-2} \text{\AA}^{-1}$) are assumed, with the option to convert from other units sometimes used by Kurucz ($\text{erg s}^{-1} \text{cm}^{-2} \text{Hz}^{-1}$).

have taken a different approach. The transmission as a function of wavelength has been determined for each optical component separately, with the instrumental transmission being the product of the components in use. The transmittances of the various optical components of the instrument are shown in Figures 2, 3, and 4. The nominal reflectivity of the telescope mirrors is also accounted for in the same way. Where possible we used a Cary 1E UV-Vis spectrometer to make measurements of the filters, modulators, and each of the other optical components in the lab, and supplement this with manufacturer data where that proved difficult. This is a better approach than using only manufacturer’s data which may not always cover the full wavelength range of HIPPI-2^d. Acquiring data for each of the components individually allows for easy and accurate adjustments when components are swapped. The flexibility of this approach has allowed us to use the one bandpass model for all HIPPI-2 observations with and without the negative achromatic lens, as well as all of our older measurements with HIPPI and Mini-HIPPI.

The modulators are designed to be half-wave retarders at one wavelength only. At other wavelengths, the modulation efficiency ($e(\lambda)$) will fall off. The raw polarisation measurements therefore need correcting by dividing by the effective efficiency given by

$$e_{\text{eff}} = \frac{\int e(\lambda)S(\lambda)d\lambda}{\int S(\lambda)d\lambda}. \tag{6}$$

For any given modulator, $e(\lambda)$ may be determined by either a lab-based calibration or through on-sky observations of objects with known polarisations. The bandpass model has a built-in option for modelling interstellar polarisation by applying either a Serkowski Law (Serkowski et al. 1975) or Serkowski–Wilking Law (Wilking et al. 1982) to the source^e. When the source spectrum and polarisation as well as the other contributors to the bandpass are well characterised, we can use a forward model to calibrate the modulator performance with a fitting routine, since

$$p = \frac{\int p_{is}(\lambda)e(\lambda)S(\lambda)d\lambda}{\int S(\lambda)d\lambda}, \tag{7}$$

where $p_{is}(\lambda)$ describes the interstellar polarisation of the source.

Prior to its first use, the ML modulator was calibrated in our laboratory using as a source the light from an incandescent bulb—which we approximate as a blackbody—collimated and directed through a polariser to produce 100% polarised light. Measurements were then made with the installed broadband filters and a number of narrowband filters. The modulation efficiency is different for high and low polarisations (see Appendix A). For a 100% polarised source, the modulation efficiency is given by

$$e(\lambda) = \frac{e_{\text{max}}}{2} \left(1 + \frac{1 - \cos(2\pi \Delta/\lambda)}{3 + \cos(2\pi \Delta/\lambda)} \right), \tag{8}$$

where e_{max} is the maximum efficiency of the unit—in theory this is 1; however, we find a value slightly less than this sometimes fits the data better. The term Δ is the optical path length of the FLC, and according to Gisler et al. (2003) is given by

$$\Delta = \frac{\lambda_0}{2} + Cd \left(\frac{1}{\lambda^2} - \frac{1}{\lambda_0^2} \right), \tag{9}$$

^dWe also identified some unadvertised long wavelength light leaks in the shortpass filters.

^eThe bandpass model also allows for the addition of source intrinsic polarisation through an input file. Additionally, the intrinsic or interstellar polarisation can be rotated arbitrarily to return predictions of q and u .

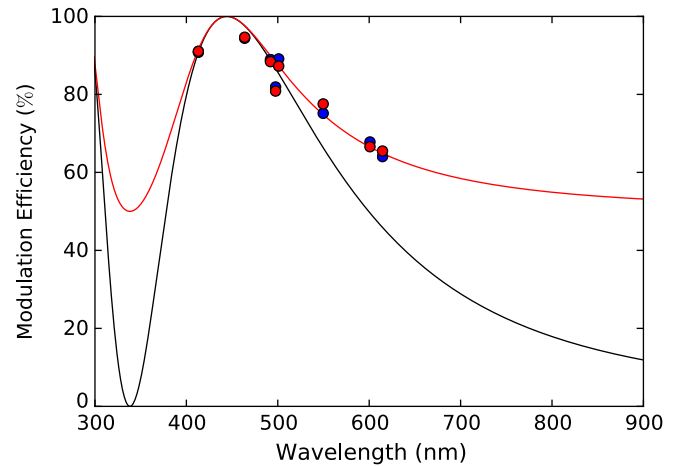


Figure 9. The laboratory data (blue dots) taken to calibrate the Meadowlark modulator is shown. The red line shows the (high-polarisation) modulation efficiency curve that best fits the data, with the red points corresponding to the exact bandpass of the data points. The black line shows the low-polarisation approximation modulation curve for the same fit parameters. The points are shown to correspond to their effective wavelength, and are left to right: 400NB, 500SP, g' , 425SP, 500NB, Clear, 600NB, r' . Although the bluer detectors were used, the 425SP effective wavelength is longer than typical owing to the extreme redness of the source (2551 ± 149 K blackbody).

where λ_0 is the wavelength of peak efficiency (i.e. the half-wave wavelength) and the terms C —describing the birefringence of the crystal—and d —the layer thickness—can be treated as a single term. Thus, the modulation efficiency can be determined as a function of wavelength by fitting e_{max} , λ_0 , Cd , and the blackbody temperature of the source, T_{bb} .

Figure 9 shows the fit obtained to the calibration data for the ML modulator; the fit parameters are given in Table 3. Also shown is the low-polarisation approximation for $e(\lambda)$. Astronomical observations made with HIPPI-2 are almost exclusively of objects for which the low-polarisation approximation (see Appendix A) is appropriate (up to 10%). In this case, the modulation efficiency is given by

$$e(\lambda) = e_{\text{max}} \left(\frac{1 - \cos(2\pi \Delta/\lambda)}{2} \right). \tag{10}$$

The BNS modulator was originally calibrated for HIPPI in early 2014 in the laboratory in a similar way to the ML unit. However, it has become apparent that its performance has changed over time with the λ_0 value in equation 9 shifting to longer wavelengths and this performance drift has accelerated. Consequently, we have since employed a different method to calibrate the modulators, where multi-band observations of high-polarisation standards are used as known sources in the calibration. In this case, it is equation (10) that is used rather than equation (8) in the bandpass model to fit the data, but otherwise the procedure is the same.

Table 4 gives details of the high-polarisation standard stars we have employed to calibrate modulator performance. Table 3 shows the parameters fit for the ML and BNS modulators used with HIPPI-2, as well as the Micron Technologies (MT) modulator previously used with HIPPI and Mini-HIPPI. The ML modulator has a bluer λ_0 than either of the other two. The BNS modulator has been used a lot; we have broken its usage down into seven eras, the last five of which correspond to HIPPI-2 runs. Clearly, λ_0 has increased over time—by ~ 100 nm. The modulator was used frequently in 2018, with over 50 nights of observing, but it is not clear

Table 3. Modulator parameters

Modulator	Era	Instrument	Data from	λ_0 (nm)	Cd ($\times 10^7$ nm ³)	e_{max}
ML		HIPPI-2	2018 Laboratory	444.2 \pm 2.7	3.163 \pm 0.476	1.000 \pm 0.021
ML	1	HIPPI-2	2018 to 2019	455.2 \pm 1.9	2.677 \pm 0.103	1.000
BNS		HIPPI	2014 Laboratory	504.6 \pm 2.4	2.277 \pm 0.175	0.977 \pm 0.009
BNS	1	HIPPI	2014 to 2015	494.8 \pm 1.6	1.738 \pm 0.060	0.977
BNS	2	HIPPI	2016 to 2017	506.3 \pm 2.9	1.758 \pm 0.116	0.977
BNS	3	HIPPI-2	2018 Jan–May	512.9 \pm 3.9	2.367 \pm 0.177	0.977
BNS	4	HIPPI-2	2018 Jul	517.5 \pm 16.1	2.297 \pm 0.924	0.977
BNS	5	HIPPI-2	2018 Aug 16–23	546.8 \pm 6.0	2.213 \pm 0.261	0.977
BNS	6	HIPPI-2	2018 Aug 24–27	562.7 \pm 4.7	2.329 \pm 0.192	0.977
BNS	7	HIPPI-2	2018 Aug 29–Sep 2	595.4 \pm 4.8	1.615 \pm 0.145	0.977
MT ^a		HIPPI	2014 Laboratory	505. \pm 5.	1.75 \pm 0.05	0.98 \pm 0.00
MT		HIPPI/MHIPPI	2014 to 2018	507.6 \pm 2.6	1.837 \pm 0.128	0.980

Notes: Errors given for parameters fit.

^a From Bailey et al. (2015), given to fewer decimal places.

Table 4. Polarised standard stars

Standard	m_V	SpT	E(B–V)	R_V	P_{max} (%)	λ_{max} (μ m)	K	PA ^a ($^\circ$)	References	Desig.
HD 23512	8.09	A0	0.36	3.3	3.2	0.61	1.02	30.0	1, 2, 3.	A
HD 80558	5.93	B6	0.60	3.35	3.34	0.597	1.33	163.3	4.	B
HD 84810	3.40	F8	0.34	3.1	1.62	0.57	1.15	100.0	2, 4.	C
HD 111613	5.72	A1	0.39	3.1 ^b	3.2	0.56	0.94	81.0	1.	D
HD 147084	4.57	A4	0.72	3.9	4.34	0.67	1.15	32.0	5, 6.	E
HD 149757	2.56	O9	0.32	3.09	1.48	0.598	1.00	127.4	7, 8.	F
HD 154445	5.61	B1	0.42	3.15	3.73	0.558	0.95	90.1	2, 4, 6.	G
HD 160529	6.66	A2	1.29	3.1	7.31	0.543	1.15	20.4	2, 4.	H
HD 161056	6.32	B1.5	0.59	3.13	4.02	0.572	1.43	67.5	9.	I
HD 187929	3.80	F6	0.18	3.1	1.76	0.56	1.15	93.8	4.	J
HD 203532	6.38	B3	0.28	3.37	1.23	0.574	1.39	127.8	9.	K
HD 210121	7.68	B7	0.31	2.42	1.38	0.434	0.55	155.4	9.	L

Notes: References: (1) Serkowski (1974), (2) Hsu & Breger (1982), (3) Guthrie (1987), (4) Serkowski et al. (1975), (5) Wilking et al. (1980), (6) Martin et al. (1999), (7) McDavid (2000), (8) Patriarchi et al. (2001), (9) Bagnulo et al. (2017).

^a PA chosen to reflect that expected in the g' filter.

^b The value of R_V is assumed, and HD 111613 has been used to calibrate PA, but not modulator performance.

Table 5. Low-polarisation standard stars

Standard	Hem ^a	m_V	SpT	d (pc)	q (ppm)	u (ppm)	References	Desig.
HD 2151	S	2.79	G0V	7.5	−8.6 \pm 2.5	−1.6 \pm 2.5	Cotton et al. (2016a)	A
HD 10700	S	3.50	G8V	3.7	1.3 \pm 3.1	0.3 \pm 3.0	Cotton et al. (2017b)	B
HD 49815	S	−1.46	A1V+DA	2.6	−3.7 \pm 1.7	−4.0 \pm 1.7	Cotton et al. (2016a)	C
HD 102647	N,S	2.13	A3Va	11.0	0.8 \pm 1.1	2.2 \pm 0.8	Bailey et al. (2010)	D
HD 102870	S	3.60	F9V	11.1	3.3 \pm 1.4	−0.1 \pm 1.4	Bailey et al. (2010)	E
HD 127762	N	3.02	A7IV	26.6	−2.8 \pm 1.6	−2.2 \pm 1.6	Bailey et al. (2010)	F
HD 128620J	S ^b	−0.10	G2V+K1V	1.3	5.7 \pm 1.9	14.4 \pm 1.9	Bailey et al. (2017)	G
HD 140573	N,S	2.63	K2IIIb	25.4	−2.3 \pm 2.9	3.9 \pm 1.0	Bailey et al. (2010)	H

Notes: ^a Indicates the hemisphere(s) in which the standard has been used.

^b HD 128620J (α Cen) is used predominantly on small telescopes where the night-to-night precision is greater than the reported polarisation.

what the cause of the performance drift is. By contrast, the MT modulator's performance is unchanged despite 5-yr use.

4.2.2. PA Correction

During a run, observations made of polarised standard stars (Table 4) in either the g' or Clear filters are used to determine the position angle alignment of the instrument. The average difference between the PA values from the literature and the PA from our measurements, denoted θ , is determined and all the data rotated according to

$$q = q_i \cos \theta + u_i \sin \theta, \quad (11)$$

$$u = u_i \cos \theta - q_i \sin \theta, \quad (12)$$

where the i subscript denotes the instrument reference frame. The precision of the literature measurements is not much better than a degree, yet typically the standard deviation (SD) of PA measurements made with HIPPI-2 is 0.5° or better.

Observations of polarised standards in other filters are made to check for wavelength-dependent effects. The PA of polarised standards can change slightly with wavelength, but any deviation, $\Delta\theta$, much larger than a degree is considered to be an instrumental effect.

The majority of the time there is no significant rotation with wavelength. However, during the 2018JUL and 2018AUG runs^f, a significant $\Delta\theta$ was detected at short wavelengths, which we infer is associated with the performance drift of the BNS modulator. For 2018AUG, $\Delta\theta$ was the greatest for the 500SP filter, 5.8° , reducing to 2.6° for the 425SP filter. The effect was similar for 2018JUL: 5.6° for 500SP and 3.3° for 425SP. Observations made in these bands are counter-rotated by a corresponding amount as a correction. For observations made in Clear with a λ_{eff} less than the mean of the g' polarised standards, a correction was calculated by fitting a parabola to the $\Delta\lambda$ and λ_{eff} values of the g' , 500SP and 425SP filters to get a function for $\Delta\theta(\lambda_{\text{eff}})$. Small corrections were also applied to 2018FEB and 2018MAR data using a similar method: 2.7° at 425SP and 1.35° at 500SP.

Similar corrections for the ML modulator have not been required for 425SP or 500SP bands, but a correction of $\Delta\theta = -14.65^\circ$ to the U band data from the 2019MAR run was required.

4.2.3. TP correction

The last correction applied is that for the TP^g. This is the zero-point correction, or the polarisation we measure when observing an unpolarised source. The telescope optics impart a small polarisation on every measurement recorded. On an equatorial telescope, we can treat this polarisation as a constant offset. While the telescope is the main cause of this zero-point offset, it is possible that when the actual TP is small there may be significant contributions to the zero-point from instrumental sources as well. For each filter, detector and aperture combination we calculate a TP in terms of q and u based on the average of low-polarisation standard stars observed. Table 5 gives a list of the standards we have employed. The list has been kept short deliberately with the aim of collecting enough comparable data on the standards to eventually determine the offsets between them—and better identify undesirable variability—but at present each is assumed to be zero to determine the TP.

^fSee Section 5 for a full description of observing runs.

^gWhen the TP is large compared to the polarised standard polarisation magnitudes, the order of the TP and PA corrections need to be swapped. When the TP is small however, performing the PA correction first has the benefit of determining the TP in the sky reference frame. TP determinations can then be combined easily from back-to-back runs where the instrument is mounted at a different PA

Although there are polarisation values given for these stars in the literature, they either come from PlanetPol observations (those from Bailey et al. 2010) where the bandpass was quite different to the typical HIPPI-2 observation, or they are from other observations we have made with this same method of determining TP. However, all of the low-polarisation stars we use are near enough to the Sun so that interstellar polarisation will be very low (Cotton et al. 2016a, 2017b) and have spectral types not associated with intrinsic polarisation (Cotton et al. 2016a,b). The furthest standards reside in a part of the northern sky found to have an interstellar polarisation per distance about an order of magnitude less than is common in the southern sky (Bailey et al. 2010; Cotton et al. 2016a, 2017b).

In the case that an observation is made and no specific standards have been observed with the same exact set-up, the combination with the same filter and detector and closest aperture size is used first. If this fails, the combination with the closest effective wavelength to the target is used instead.

5. Instrument performance

The performance of HIPPI-2 has been evaluated based on observations obtained during 2018 and early 2019 on three telescopes. Observations with the WSU 60-cm telescope were obtained on 2018 January 23, May 4–5 and 9–11, and 2019 February 11–15. Observations with the 3.9-m AAT were obtained on 2018 February 1–5, March 23–April 8, June 10–25, August 16–September 2, and 2019 March 15–26. Observations with the Gemini North telescope were obtained in Director's Discretionary time on 2018 July 4–6. Table 6 lists the telescope and instrument configurations for each run. In the following discussion, we refer to the individual runs using the names given in the first column of Table 6.

5.1. Throughput

HIPPI-2 improves on the optical throughput of HIPPI through the use of a simpler optical system and the use of more efficient filters. Using the bandpass model described in Section 4.2.1, we find that the expected improvement in instrument throughput amounts to about 20% in Clear and about 65% in the g' filter. Inspection of the measured intensity in actual AAT observations indicates the real improvement is a little better than these figures predict. Additional gains probably come from the improved telescope throughput due to the use of the $f/15$ secondary which has a smaller central obstruction than the $f/8$ configuration used with HIPPI, as well as from the ability to use larger apertures with HIPPI-2 that eliminate any spillage of light due to seeing.

5.2. Telescope polarisation

Measurements of the zero-point correction (or TP) were made by observing low-polarisation standard stars as described in Section 4.2.3. Results for the the equatorially mounted telescopes (AAT and WSU) are listed in Tables 7 and 8. A unique TP determination was made for each filter and aperture combination used. For each telescope and each run set, the individual TP determinations are listed in order of effective wavelength. For most measurements, the TP magnitude is the greatest in the bluest wavelength bands. The TP PA is very similar between bands most of the time, but does appear to rotate slightly away from the mean in the bluest bands—the low TP in 2018JUL/AUG and 2019MAR accentuates this rotation.

Table 6. Summary of Runs for HIPPI-2

Run	S/R ^a	Run duration (UT)	Tel.	Focus (f/)	Mod.	Comments
2018JAN		2018 Jan 23	WSU	10.5*	BNS-E3	WSU Commissioning Run.
2018FEB	A	2018 Feb 02	AAT	15	BNS-E3	AAT Commissioning Run.
	B	2018 Feb 03				Back-end adjustment.
	C ^b	2018 Feb 04				Back-end adjustment.
	D ^b	2018 Feb 04 to 2018 Feb 05				Alignment adjusted.
2018MAR		2018 Mar 23 to 2018 Mar 07	AAT	8*	BNS-E3	Back-end redesigned.
2018MAY		2018 May 04 to 2018 May 11	WSU	10.5*	BNS-E3	
2018JUN		2018 Jul 04 to 2018 Jul 06	Gemini Nth	16	ML-E1	Clone instrument. ^d
2018JUL ^c		2018 Jul 10 to 2018 Jul 25	AAT	8*	BNS-E4	Rapid modulator evolution.
2018AUG ^c		2018 Aug 16 to 2018 Aug 23	AAT	8*	BNS-E5	Rapid modulator evolution.
		2018 Aug 24 to 2018 Aug 27			BNS-E6	Rapid modulator evolution.
		2018 Aug 29 to 2018 Aug 02			BNS-E7	Rapid modulator evolution.
2019FEB		2019 Feb 11 to 2019 Feb 15	WSU	10.5*	ML-E1	
2019MAR		2019 Mar 15 to 2019 Mar 26	AAT	15	ML-E1	650LP replaced with U.

Notes: * Indicates a focal configuration requiring the use of the negative achromatic lens—the effective focal ratio is $f/$ twice the number given. The two different focal arrangements on the AAT use different secondary mirrors.

^a S/R indicates a subrun, that is, where the instrument has been removed from the telescope mid-run and then remounted. Ordinarily, this operation requires a new PA calibration, but allows TP measurements to be combined. However, for the 2018FEB-B and 2018FEB-C runs, the instrument was altered compared to the previous subrun and new TP calibrations were acquired.

^b and ^c indicate that the TP has been combined between these runs or subruns, this is possible where the instrument and telescope performance is stable.

^d The clone is a complete copy of the original instrument. The aperture wheel is 3D printed and varies between units; nominal aperture sizes have been assumed for the 2018JUN run. The clone instrument used a different pair of blue PMT units for the 2018JUN run than have otherwise been used with HIPPI-2; these PMTs were used for early HIPPI runs.

Table 7. Telescope polarisation by Run at WSU with HIPPI-2

Run ^a	Fil	PMT	Ap (arcsec)	λ_{eff} (nm)	Standard observations								$p \pm \Delta p$ (ppm)	$PA \pm \Delta PA$ (°)
					A	B	C	D	E	F	G	H		
2018JAN	Clear	B	58.9	469.6	0	0	3	0	0	0	0	0	41.4 ± 2.6	128.3 ± 1.8
2018MAY	g'	B	58.9	464.9	0	0	4	0	0	0	0	0	25.4 ± 2.6	82.8 ± 2.9
2018MAY	Clear	B	58.9	473.4	0	0	6	5	0	0	0	0	27.7 ± 2.0	92.8 ± 2.0
2018MAY	Clear	R	58.9	601.9	0	0	0	0	0	1	0	0	33.7 ± 3.9	79.1 ± 3.2
2019FEB	g'	B	58.9	463.1	0	0	4	0	0	0	0	0	23.9 ± 1.7	28.9 ± 2.0
2019FEB	Clear	B	58.9	467.3	0	0	3	0	0	0	0	0	12.1 ± 3.1	47.1 ± 7.6

Notes: The key for the letters denoting the low-polarisation standards is in Table 5.

As noted in Section 4.2.3, while the TP is the main contributor to the zero-point polarisation measured with HIPPI-2 there are likely to be small contributions from residual instrumental effects as well. One example of this is that there are minor differences between TP measured in the same band but with different apertures. In part, this may be due to using different standard stars. However, we believe there are other significant factors. During the 2018MAR run, we used different centring strategies for the different aperture sizes. In the two smallest apertures, the standards were re-centred at each PA; in the larger apertures, centring was performed only at PA = 0°. This may lead to small zero-point offsets due to the centring effects described in Section 5.4

The TP recorded on the WSU telescope has always been very low—between about 10 to 40 ppm. This compares favourably to the University of New South Wales (UNSW) telescope where the TP has been around 60 to 90 ppm (Bailey et al. 2017, 2019). The small differences between runs might be down to refinements we

have made to the way the instrument is mounted over time, or it could be related to the dust pattern on the mirrors. Regardless, there have been no significant shifts during a run.

In Figure 10, all the TP measurements made with HIPPI and HIPPI-2 at the $f/8$ focus of the AAT in both g' and r' bands (which are the most consistently observed filter bands) are plotted. The grey vertical lines represent realuminisation of the primary mirror. A number of observations can be made. The magnitude of the TP is usually lower in g' than r' ; this is consistent with what we see in Table 8. The magnitude of the TP was reduced at every realuminisation from 2014 to 2017 where it reached around 10 ppm. The magnitude of the TP tends to increase with time following realuminisation—this can reasonably be ascribed to the inevitable buildup of dust on the main mirror with time. The TP PA has been fairly consistent, with the exception of the 2018MAR run, which is probably reflective of the contribution to the TP of the secondary mirror. The 2018MAR result can most easily be explained by

Table 8. Telescope polarisation by run at the AAT with HIPPI-2

Run	Fil	PMT	Ap (arcsec)	λ_{eff} (nm)	Standard Observations								$\rho \pm \Delta\rho$ (ppm)	$PA \pm \Delta PA$ ($^\circ$)
					A	B	C	D	E	F	G	H		
2018FEB-A	g'	B	16.8	464.3	0	0	0	0	1	0	0	0	225.4 \pm 3.8	88.1 \pm 0.5
2018FEB-B	425SP	B	16.8	399.0	0	0	1	0	0	0	0	0	303.6 \pm 3.0	91.4 \pm 0.3
2018FEB-B	g'	B	16.8	463.5	0	0	2	1	0	0	0	0	192.6 \pm 1.1	88.1 \pm 0.2
2018FEB-B	Clear	B	16.8	467.0	0	0	2	1	0	0	0	0	190.5 \pm 1.0	88.7 \pm 0.2
2018FEB-B	Clear	B	9.2	467.2	0	0	2	1	0	0	0	0	186.4 \pm 1.1	86.8 \pm 0.2
2018FEB-B	r'	B	16.8	602.6	0	0	1	0	0	0	0	0	129.6 \pm 2.0	88.1 \pm 0.4
2018FEB-C/D	500SP	B	16.8	434.7	0	0	1	0	0	0	0	0	215.6 \pm 1.0	90.0 \pm 0.1
2018FEB-C/D	g'	B	16.8	463.6	0	0	5	3	0	0	0	0	178.9 \pm 0.7	87.7 \pm 0.1
2018FEB-C/D	Clear	B	16.8	469.5	0	0	5	3	1	0	0	0	179.7 \pm 0.8	87.7 \pm 0.1
2018FEB-C	g'	R	16.8	481.8	0	0	1	0	0	0	0	0	168.7 \pm 0.9	81.2 \pm 0.2
2018FEB-C	r'	R	16.8	622.2	0	0	1	0	0	0	0	0	109.0 \pm 1.2	86.3 \pm 0.3
2018FEB-C	650LP	R	16.8	720.7	0	0	1	0	0	0	0	0	81.2 \pm 1.9	90.3 \pm 0.7
2018MAR	425SP	B	15.7	403.0	0	0	3	3	3	0	0	0	183.1 \pm 2.8	4.0 \pm 0.4
2018MAR	500SP	B	15.7	440.9	0	0	3	3	3	0	0	0	145.5 \pm 1.2	4.0 \pm 0.2
2018MAR	g'	B	15.7	466.3	0	0	3	3	3	0	0	0	130.0 \pm 0.9	0.9 \pm 0.2
2018MAR	Clear	B	8.6	471.3	0	0	2	3	0	0	0	0	114.8 \pm 0.7	178.7 \pm 0.2
2018MAR	Clear	B	5.3	472.9	0	0	0	3	0	0	0	0	125.1 \pm 1.3	177.2 \pm 0.3
2018MAR	Clear	B	15.7	485.1	0	0	4	4	3	0	0	5	130.8 \pm 0.7	1.2 \pm 0.1
2018MAR	V	B	15.7	533.2	0	0	3	0	0	0	0	0	125.6 \pm 0.8	2.5 \pm 0.2
2018MAR	r'	R	15.7	623.3	0	0	2	3	2	0	0	0	113.6 \pm 1.4	1.8 \pm 0.4
2018MAR	650LP	R	15.7	722.3	0	0	2	3	2	0	0	0	107.8 \pm 1.9	2.8 \pm 0.5
2018JUL/AUG	425SP	B	11.9	407.3	3	2	2	0	1	0	0	3	19.8 \pm 6.2	49.7 \pm 9.4
2018JUL/AUG	500SP	B	11.9	445.0	2	2	2	2	1	0	0	2	18.6 \pm 1.4	41.2 \pm 2.2
2018JUL/AUG	g'	B	11.9	470.4	3	3	2	2	1	0	0	2	13.6 \pm 1.1	80.9 \pm 2.2
2018JUL/AUG	Clear	B	11.9	489.4	3	3	2	2	2	0	0	2	10.6 \pm 0.9	79.6 \pm 2.6
2018JUL/AUG	V	B	11.9	537.9	1	1	2	0	1	0	0	2	20.7 \pm 1.5	87.0 \pm 2.1
2018JUL/AUG	r'	B	11.9	605.4	1	2	2	0	1	0	0	3	18.6 \pm 1.4	81.3 \pm 2.8
2018JUL/AUG	r'	R	11.9	625.6	4	2	0	2	2	0	0	1	12.5 \pm 1.2	88.5 \pm 2.7
2018JUL/AUG	650LP	R	11.9	725.7	3	2	0	2	2	0	0	1	8.1 \pm 1.9	75.8 \pm 7.0
2019MAR	U	B	12.7	380.6	0	0	2	2	0	0	0	1	103.7 \pm 7.6	88.4 \pm 2.1
2019MAR	425SP	B	12.7	398.3	0	0	2	0	0	0	0	0	4.7 \pm 1.1	56.1 \pm 7.1
2019MAR	500SP	B	12.7	434.4	0	0	1	1	0	0	0	0	67.3 \pm 2.1	110.0 \pm 0.9
2019MAR	g'	B	12.7	462.9	0	0	3	2	0	0	0	0	9.5 \pm 0.8	79.3 \pm 2.1
2019MAR	Clear	B	12.7	464.0	0	0	3	0	0	0	0	0	9.7 \pm 1.1	36.3 \pm 3.1
2019MAR	V	B	12.7	540.5	0	0	0	0	0	0	0	1	21.3 \pm 6.5	37.5 \pm 9.1
2019MAR	r'	B	12.7	602.6	0	0	1	0	0	0	0	0	13.1 \pm 5.6	105.1 \pm 14.1

Notes: The key for the letters denoting the low-polarisation standards is in Table 5.

During each run, one aperture setting is chosen as a default, with which most observations are made. We have omitted from this table TP determinations made in other apertures where only a single observation was made.

the primary mirror being marked prior to the run^h since the TP returns to a normal level following realuminising. If instrumental polarisation was contributing more, then we would expect the PA in 2017 to be different to all the 2018 runs corresponding to the change from HIPPI to HIPPI-2.

^hPossibly on March 7 when the f/15 secondary was removed for realuminising. This coating was of poor quality, which is why f/8 was used for 2018MAR.

The TP was also very high during the 2018FEB run. The PA is 90° different to the similarly high 2018MAR run, suggesting a different cause. We ascribe this to the condition of the f/15 secondary mirror, which is rarely used. The AAT primary mirror is usually realuminised every year. The f/8 secondary mirror was last realuminised in 2004, and prior to the 2019MAR run it had been more than 20 yr since the f/15 secondary was realuminised (S. Lee, priv. comm.). While the f/8 secondary is always well protected from

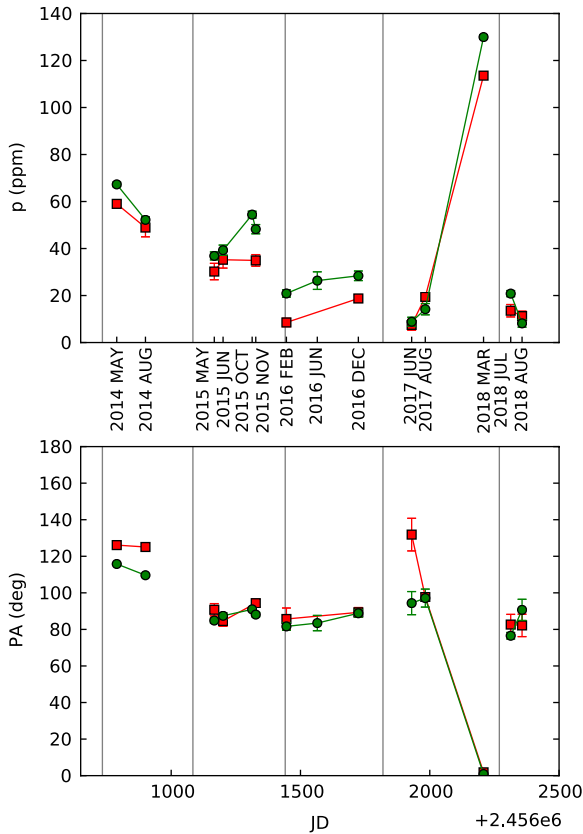


Figure 10. Telescope polarisation (TP) at the AAT f/8 focus in two bands: g' (green circles) and r' (red squares) plotted against time (JD). The upper panel shows the magnitude of the polarisation, while the lower panel shows the position angle. The run designations are given between the two panels. The vertical grey lines show when the primary mirror was realuminised. The HIPPI data and some of the HIPPI-2 data shown here and/or reported in Table 8 have been previously reported (Bailey et al. 2015; Cotton et al. 2016a; Marshall et al. 2016; Bott et al. 2016; Cotton et al. 2017a,b; Bott et al. 2018; Cotton et al. 2019a,b; Bailey et al. 2019), but the data have been reprocessed to benefit from refinements in the software.

falling dust, the $f/15$ secondary shares a mounting with the $f/36$ secondary and has occasionally been in an upward facing position without the side dust covers installed. The $f/15$ secondary was realuminised in March 2018 and again in September 2018. This explains why the TP is much lower in the 2019MAR run than it was for the earlier runs.

5.3. Polarisation precision

The polarisation precision achievable with HIPPI-2 has been evaluated by making repeat observations of bright low-polarisation stars in the same way as the analysis of HIPPI presented by Bailey et al. (2015). Amongst the stars used for this analysis are many of our low-polarisation standards, as well as a number of other stars with small polarisations unlikely to be variable. Table 9 shows such measurements made at the AAT during the 2018MAR run using a 15.7-arcsec aperture; the observations are grouped by filter band. In the table alongside the error-weighted mean of the Stokes q and u values are the associated SDs, σ , and the average internal error of the individual measurements, δ .

The values of σ are a conservative estimate of the precision we are achieving. However, they will tend to underestimate our ultimate precision as they include a contribution from the internal statistical error of each measurement. To attempt to allow

for this, we also calculate what we refer to as the error variance, calculated as:

$$e = \begin{cases} \sqrt{\sigma^2 - \delta^2} & \sigma > \delta \\ 0 & \sigma \leq \delta \end{cases} \quad (13)$$

We use the subscript p to denote the mean of q and u determinations of σ and e . e_p is thus an estimate of the precision we would expect to see in repeat observations if the internal errors were very small. This metric deals poorly with individual instances where $\sigma < \delta$, and is thus most useful only when examining the mean of many measurements. Based on the e_p values in Table 9, HIPPI-2 is most precise in the reddest pass band, achieving better than 1 ppm precision with the 650LP filter (based on four stars). At bluer wavelengths, the precision is still very good—2.5 ppm in g' , 6.7 ppm in 500SP. However, in the bluest band, 425SP, the precision worsens to 13.7 ppm. When used without a filter (Clear), 3.5 ppm precision is being achieved.

Observations of Sirius (HD 48915) have a systematically worse precision during the 2018MAR run than the other stars shown in Table 9. The reasons for this are unclear. If we remove the Sirius observations, the mean e_p values for the bands are 11.6, 6.2, 1.7, and 2.9 ppm for 425SP, 500SP, g' , and Clear bands, respectively.

The reported precision of HIPPI at the AAT (Bailey et al. 2015) was 4.3 ppm based on combined measurements of σ made in the g' and 500SP bands; HIPPI-2 appears to be doing slightly better than this. In Table 10, we compare the HIPPI-2 AAT precision measurements with a similar analysis of HIPPI data from 2014 to 2017. We have made relatively few sets of repeat observations in redder bands, so these are combined in the table to give a meaningful comparison. It can be seen from Table 10 that HIPPI-2 outperforms HIPPI for most bands in terms of both the σ_p and e_p measurements.

In part that may be due to the use of a larger aperture. Table 11 shows precision determinations made without a filter for the same target (β Leo) with different aperture sizes. The precision is seen to improve with increasing aperture size. Although typically around 2 arcsec or better, the seeing at the AAT can often reach 5 arcsec and is occasionally much worse. Under such conditions, a significant fraction of the light would fall outside of HIPPI's 6.9 arcsec aperture. Thus, a larger aperture improves things for bright stars where the increased sky background is not significant.

Table 12 presents precision measurements made during runs at WSU—the 2018MAY and 2019FEB runs in Clear and with an g' filter. It can be seen that the precision measured as either σ_p or e_p is not as good as that at the AAT.

5.4. What limits the precision?

Based on the results given above, we can consider what is limiting the precision achievable with these FLC-based instruments. We believe the main limitations are set by the instrumental polarisation that is inherent in this instrument design. As discussed in Bailey et al. (2015), these instruments have a large (1000's of ppm) instrumental polarisation which is intrinsic to the modulators. We largely eliminate this instrumental polarisation by rotating the modulator relative to the rest of the instrument so that the instrumental polarisation is orthogonal to the Stokes parameter being measured (this is an adjustment done when the instrument is first set up for each run). Residual effects are cancelled by the second-stage chopping procedure of repeating observations at 90° separated angles (see Section 3).

Table 9. Precision from repeat observations of bright stars with HIPPI-2 at the AAT

Star	n	λ_{eff} (nm)	$q \pm \Delta q$ (ppm)	σ_q	δ_q	e_q	$u \pm \Delta u$ (ppm)	σ_u	δ_u	e_u	σ_p	e_p
<i>425SP (B)</i>												
HD 48915	3	401.4	14.6 ± 2.2	34.7	3.9	34.5	7.9 ± 2.2	14.3	3.9	13.7	24.5	24.1
HD 50241	3	403.2	99.2 ± 6.5	4.3	11.4	0.0	47.7 ± 6.3	3.4	11.0	0.0	3.8	0.0
HD 80007*	3	398.4	-45.6 ± 2.1	3.7	3.5	0.0	14.7 ± 2.2	3.8	13.3	12.8	8.4	6.4
HD 97603	5	402.9	36.0 ± 3.7	31.4	8.5	30.2	-24.2 ± 3.7	27.3	8.4	26.0	29.3	28.1
HD 102647	3	402.3	13.0 ± 3.8	7.7	6.5	4.1	-3.4 ± 3.7	21.9	6.4	20.9	14.8	12.5
HD 102870	3	405.3	-26.3 ± 7.7	10.2	13.4	0.0	-3.9 ± 7.6	25.6	13.2	21.9	17.9	11.0
		403.0									16.5	13.7
<i>500SP (B)</i>												
HD 48915	3	437.7	-6.8 ± 0.9	6.7	1.5	6.6	-2.5 ± 0.9	9.4	1.6	9.2	8.1	7.9
HD 97603	3	440.8	21.5 ± 2.1	4.7	3.6	3.0	-7.3 ± 2.0	10.6	3.5	10.1	7.7	6.5
HD 102647	3	439.2	10.2 ± 1.6	8.1	2.8	7.6	-3.4 ± 1.7	7.1	3.0	6.4	7.6	7.0
HD 102870	3	445.7	-4.2 ± 3.2	11.8	5.5	10.5	5.6 ± 3.2	5.3	5.5	0.0	8.6	5.2
		440.9									8.0	6.7
<i>g' (B)</i>												
HD 48915	3	463.4	-10.9 ± 0.7	9.2	1.1	9.2	-3.1 ± 0.7	5.6	1.1	5.4	7.4	7.3
HD 48915*	3	462.5	3.8 ± 0.8	1.8	0.8	0.0	3.5 ± 0.7	1.3	3.5	3.3	2.1	1.6
HD 50241	5	466.2	37.6 ± 1.2	2.3	2.7	0.0	21.9 ± 1.2	4.6	2.7	3.7	3.4	1.8
HD 80007	4	464.0	-6.6 ± 0.9	3.4	1.8	2.8	16.8 ± 0.9	3.6	1.9	3.1	3.5	2.9
HD 97603	4	466.2	20.4 ± 1.4	3.9	2.8	2.7	-9.6 ± 1.4	2.5	2.8	0.0	3.2	1.3
HD 102647	3	465.0	6.0 ± 1.3	3.8	2.3	3.0	-3.6 ± 1.3	2.8	2.2	1.7	3.3	2.3
HD 102870	3	470.5	4.8 ± 2.6	2.5	4.4	0.0	6.7 ± 2.6	0.9	4.5	0.0	1.7	0.0
		465.6									3.5	2.5
<i>V (B)</i>												
HD 48915	3	533.2	-0.1 ± 0.9	1.9	1.6	1.0	-0.6 ± 0.9	6.8	1.5	6.6	4.3	3.8
<i>r' (R)</i>												
HD 102647	3	622.6	2.1 ± 2.0	2.6	3.5	0.0	3.8 ± 2.1	2.1	3.6	0.0	2.4	0.0
<i>650LP (R)</i>												
HD 50241	3	722.5	-23.1 ± 3.9	6.5	6.7	0.0	18.3 ± 4.0	6.7	6.9	0.0	6.6	0.0
HD 97603	3	721.9	8.0 ± 3.6	2.5	6.2	0.0	-4.9 ± 3.6	2.5	6.2	0.0	2.5	0.0
HD 102647	3	721.4	4.0 ± 2.9	7.0	5.1	4.8	4.7 ± 2.9	0.8	5.1	0.0	3.9	2.4
HD 175191	3	719.0	-43.7 ± 2.8	2.3	4.8	0.0	-209.5 ± 2.7	5.0	4.8	1.4	3.6	0.7
		721.2									4.2	0.8
<i>Clear (B)</i>												
HD 48915	4	469.4	-13.2 ± 0.5	8.0	1.0	7.9	-7.1 ± 0.5	4.2	1.0	4.1	6.1	6.0
HD 48915*	3	464.3	-1.9 ± 1.0	2.0	4.9	4.5	-0.7 ± 1.0	2.0	2.3	1.0	3.6	2.8
HD 102647	4	473.0	6.9 ± 1.0	2.3	2.1	1.0	-1.6 ± 1.0	4.1	2.1	3.5	3.2	2.3
HD 102870	3	489.3	3.8 ± 2.4	4.8	4.1	2.5	7.8 ± 2.3	0.8	4.0	0.0	2.8	1.3
HD 140573	5	504.6	1.5 ± 1.4	5.2	3.0	4.2	2.6 ± 1.3	6.6	3.0	5.9	5.9	5.0
		481.3									4.3	3.5

Notes: All values of σ , δ and e are in ppm.

B and R designations given parenthetically indicate which PMT was used.

* Indicates 2019MAR run (ML-E1 modulator), all other observations were from the 2018JUL/AUG run (BNS-E4-7 modulator).

Table 10. A comparison of the precision of HIPPI and HIPPI-2 on the AAT by band

Band	HIPPI-2			HIPPI		
	N	σ_p	e_p	N	σ_p	e_p
425SP ^a	5	16.5	13.7	4	21.2	13.2
500SP ^a	4	8.0	6.7	2	9.6	7.5
g' ^{ab}	7	3.5	2.5	3	4.4	2.1
Clear ^a	6	4.3	3.5	6	6.1	4.7
Redder ^c	6	3.5	1.1	3	3.1	1.6

Notes: All values of σ and e are in ppm.

^a If we remove the Sirius observations from the HIPPI-2 results, the mean e_p (N) values for the bands are 11.6 ppm (4), 6.2 ppm (3), 1.7 ppm (5), and 2.9 ppm (3) for 425SP, 500SP, g', and Clear bands, respectively.

^b Includes observations made in two different versions of the g' filter with HIPPI.

^c Combined V, r' (with both B and R PMTs), and 650LP data.

We suspect that there is a small spatial variation of this instrumental polarisation across the modulator probably associated with the fringing effects described by Gisler et al. (2003). This means that the measured polarisation could be different if the star is not precisely centred in the instrument aperture. Such an effect can explain the differences between precision on different telescopes. The AAT has very good tracking and we normally autoguide using an off-axis guide star. At the WSU telescope, we are not able to autoguide. On the UNSW, 35-cm Celestron telescope used with Mini-HIPPI centring of objects is difficult due to backlash in the telescope drives. The precision we obtain on Mini-HIPPI measured using observations of HD 49815 or HD 128620 in the Clear band is $\sigma_p = 19.8$ ppm and $e_p = 14.0$ ppm. It therefore seems likely that the poorer precision obtained with the smaller telescopes is due to poorer tracking leading to errors in centring of the stars.

During the 2018MAR AAT observing run, we made a number of short measurements of Sirius to determine the effect miscentring has. For this purpose, the 2.6-mm (11.9 arcsec) aperture was used, and the results read from the on-screen quick-look polarisation determination. Measurements were acquired at two orthogonal PAs with both the g' and 425SP filter. The star was first centred in the normal way, and then off-set in 2 arcsec increments either side of centre. A representative efficiency correction was made to the measurements, and the results are shown in Figure 11 as the difference between the measurement at centre and each subsequent measurement.

There is a trend such that the further off centre the target is, the greater is the likely deviation from the centred value. The effect is much more pronounced in the 425SP band than the g' band, so this confirms our suspicions and also helps to explain why the precision of HIPPI and HIPPI-2 is poorer at blue wavelengths.

5.5. Performance versus magnitude

In Figure 12, we show the error in polarisation, as determined by the data reduction system, plotted against the B magnitude of the object observed. For this purpose, we selected observations obtained in good sky conditions in the Clear and g' filters. The errors have been scaled to a fixed integration time (T) of 1000 s under the assumption that the error varies as $T^{-0.5}$. The results scale with magnitude in the way expected for photon-shot-noise-limited performance as shown by the lines in the diagram. The dependence on telescope aperture is also as expected.

However, it can be seen that for very bright stars, the performance is relatively poorer, with the points lying above the line. This was also seen in the similar plot for Mini-HIPPI (Bailey et al. 2017). Comparison of the curves for different telescopes suggest

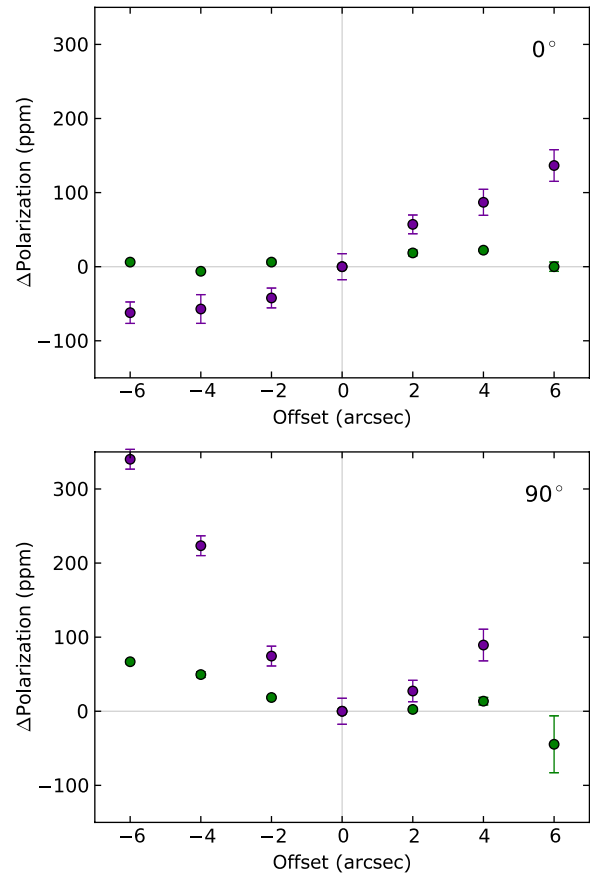


Figure 11. The difference between polarisation recorded from a measurement in a centred and offset position at a PA of 0° (top) and 90° (bottom). The data points are colour coded according to the filter: g' (green), 425SP (violet). Not shown is the 425SP value for 90° at an offset of 6 arcsec which was -894 ± 162 ppm, indicating it was very near the edge of the aperture.

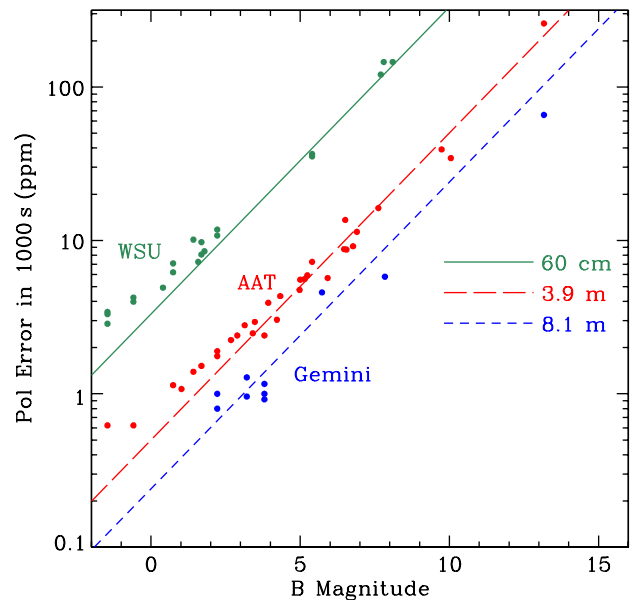


Figure 12. Internal errors of observations with HIPPI-2 scaled to an integration time of 1000 s and plotted against B magnitude. The lines which are fitted through the fainter observations have the slope expected for photon noise limited observations and are spaced by the scaling factors expected for the change in collecting area of the three different telescopes.

Table 11. Precision in different sized aperture observations of HD 102647 made with no filter

Aperture	n	λ_{eff} (nm)	$q \pm \Delta q$ (ppm)	σ_q	δ_q	e_q	$u \pm \Delta u$ (ppm)	σ_u	δ_u	e_u	σ_p	e_p
5.3 arcsec	3	472.9	-0.4 ± 1.4	7.0	2.5	6.6	0.5 ± 1.5	6.2	2.6	5.7	6.6	6.1
8.6 arcsec	3	472.9	4.5 ± 1.2	8.0	2.1	7.7	1.3 ± 1.2	2.9	2.1	2.0	5.4	4.8
15.7 arcsec	4	473.0	6.9 ± 1.0	2.3	2.1	1.0	-1.6 ± 1.0	4.1	2.1	3.5	3.2	2.3

Notes: All values of σ , δ , and e are in ppm.

Table 12. Precision from repeat observations of bright stars with HIPPI-2 at WSU

Star	n	λ_{eff} (nm)	$q \pm \Delta q$ (ppm)	σ_q	δ_q	e_q	$u \pm \Delta u$ (ppm)	σ_u	δ_u	e_u	σ_p	e_p
<i>g'</i>												
HD 48915	4	464.9	-0.8 ± 2.9	7.9	5.9	5.1	-0.9 ± 2.8	9.8	5.7	8.0	8.8	6.5
HD 48915*	4	463.1	-2.8 ± 1.7	9.8	3.7	9.1	-3.2 ± 1.6	13.9	3.6	13.4	11.9	11.3
HD 80007	3	464.4	-8.1 ± 5.3	12.7	9.6	8.4	7.6 ± 5.0	10.4	9.1	5.0	11.6	6.7
		464.6									10.8	8.2
<i>Clear</i>												
HD 48915	6	471.7	-1.7 ± 1.5	10.5	3.8	9.7	11.0 ± 1.5	14.5	3.8	14.0	12.5	11.9
HD 48915*	3	467.3	2.1 ± 3.3	10.0	6.2	7.9	0.6 ± 3.2	3.3	6.0	0.0	6.7	3.9
HD 80007	6	470.8	-5.0 ± 2.9	4.1	7.3	0.0	21.6 ± 2.9	11.2	7.2	8.6	7.7	4.3
HD 102647	5	475.3	4.0 ± 4.1	9.9	9.2	3.6	-14.5 ± 4.1	17.2	9.1	14.6	13.6	9.1
		472.6									10.1	7.3

Notes: All values of σ , δ , and e are in ppm. * Indicates 2019FEB run (ML-E1 modulator), all other observations were from the 2018MAY run (BNS-E3 modulator).

that the points start to deviate from the line at a similar magnitude ($B \sim 3$), rather than at a similar signal level. This suggests that the effect is not due to instrumental noise sources such as those from the PMT. However, it is consistent with the idea that scintillation noise on bright stars becomes significant and is not completely removed by our 500-Hz modulation frequency (Bailey et al. 2017).

5.6. Position angle precision

As described in Section 4.2.2, PA is calibrated by comparing g' and Clear measurements of the polarised standards listed in Table 4 with their literature values to determine ΔPA . The uncertainties in the literature values are typically of order a degree. Within this limitation, HIPPI-2's precision in PA can be gauged by looking at the SD of ΔPA for each run; this is done in Table 13.

With the exception of the 2018JUL observing run all the SDs fall within a degree, which is about as good as can be expected. However, HIPPI performed a little better by the same measure (Bailey et al. 2019). It is noteworthy that the SDs are largest for 2018JUL and 2018AUG when the modulator performance was drifting, and also for 2018JUN on Gemini North where the TP is very large and difficult to model (see Section 5.8). Without these difficulties, it is reasonable to expect that PA calibration will be able to be performed as well with HIPPI-2 as with HIPPI, and that the in-run repeatability will be limited only by the precision of the rotator and rotator control software.

The determined PA for HD 203532 in g' of $125.2 \pm 0.9^\circ$ from the 2018JUL run is unusually low compared to its literature value of 127.8° (Bagnulo et al. 2017). It was also observed in other filters during two different acquisitions, and the PA is consistent with the g' observation. So, the observation is not a rogue, but represents a clear difference to the literature.

Table 13. Precision in PA by Observing Run

Run	S/R	Standard Observations												SD (°)	
		A	B	C	D	E	F	G	H	I	J	K	L		
2018JAN		0	0	<i>1</i>	0	0	0	0	0	0	0	0	0	0	-
2018FEB	A	0	0	1	0	0	0	0	0	0	0	0	0	0	-
2018FEB	B	0	1	0	0	0	0	0	0	0	0	0	0	0	-
2018FEB	C	0	2	0	0	0	0	0	0	0	0	0	0	0	0.08
2018FEB	D	0	1	0	0	0	0	0	0	0	0	0	0	0	-
2018MAR		0	1	0	1	1	0	0	0	0	1	0	0	0	0.26
2018MAY		0	0	0	0	2	0	0	0	0	0	0	0	0	0.15
2018JUN		0	0	0	0	1	0	1	0	1	0	0	2	0	0.80
2018JUL		0	0	0	0	1	0	1	1	0	0	1	0	0	^a 1.56
2018AUG		0	0	0	0	3	0	0	3	0	5	0	0	0	0.86
2019FEB		0	0	1	0	1	0	0	0	0	0	0	0	0	0.11
2019MAR		0	1	1	0	1	0	0	0	0	0	0	0	0	0.46

Notes: The key for the letters denoting the low-polarisation standards is in Table 4. All standards were observed in g' except the following which were observed in Clear: All from 2018JAN, 1x HD 80558 (Standard B) from 2018FEB C, All from 2018MAY, 1x HD 120121 (Standard L) from 2018JUN, 1x HD 187929 (Standard J) from 2018AUG—which have all been italicised in the table.

^a If HD 203532 (Standard K) is excluded: 0.93.

5.7. Accuracy

The accuracy of HIPPI-2 on high-polarisation objects can be gauged by comparing observations made of high-polarisation standards with predictions made by the bandpass model. In Table 14, all the high-polarisation standard observations made with HIPPI-2 regardless of the instrument configuration of telescope are grouped by band—the filter and PMT combination—

Table 14. Accuracy by band

Band		λ_{eff} (nm)	Standard observations												Obs./Pred.	
Fil	PMT		A	B	C	D	E	F	G	H	I	J	K	L	Mean	SD
<i>All observations</i>																
U	B	381.7	0	1	0	0	1	0	0	0	0	0	0	0	1.124	0.004
425SP	B	404.2	0	1	0	0	3	1	1	2	1	3	1	1	1.031	0.081
500SP	B	441.5	0	0	0	0	2	0	2	2	1	2	1	1	1.013	0.058
g'	B/R	473.9	0	5	3	1	8	1	2	4	1	6	1	1	0.995	0.060
Clear	B	481.6	0	1	1	0	2	3	0	0	0	1	0	1	1.015	0.063
V	B/R	541.0	0	0	0	0	1	1	1	2	0	2	1	0	1.001	0.066
500SP	R	552.2	0	0	0	0	1	0	0	0	0	1	0	0	0.988	0.031
r'	B	605.0	0	0	0	0	3	0	3	2	1	2	1	1	1.033	0.083
r'	R	626.3	0	1	0	0	1	1	0	1	0	1	0	0	0.997	0.023
425SP	R	714.5	0	0	0	0	1	0	0	1	0	1	0	0	0.923	0.021
650LP	R	730.2	0	1	0	0	1	1	0	1	0	1	0	0	1.049	0.031
<i>Selected observations</i>																
g'	B/R	472.7	0	5	3	1	4	0	1	1	0	2	0	0	1.011	0.045

Notes: The mean and SD are in ratio units. The key for the letters denoting the low-polarisation standards is in Table 4. Selected observations exclude runs 2018JUN and 2018AUG, HD 149757 and HD 203532.

and the average and SD of the ratio of observation to prediction reported. In this case, the predictions are calculated assuming purely interstellar polarisation based on the literature values given in Table 4. It should be noted that there are reports of polarisation variability in a number of these polarisation standards (Bastien et al. 1988).

In the majority of bands, the mean observed polarisation is within 1.5% of that calculated by the bandpass model. This is not surprising given that the same standards were used to calibrate the modulator curves. However, the discrepancy is larger for bands corresponding to the edge of the PMT response curves at the red end or the rapid drop-off in modulator efficiency at the blue end. In particular, it is noteworthy that the combination of the r' filter and the blue-sensitive PMT corresponds to both a comparatively large mean discrepancy, 3.3%, and a large SD of 8.3%, while the combination of the r' filter and the red-sensitive PMT results in much more favourable measures. The most likely explanation is that the PMT response curves are not accurate at the extremes of their range. The optical components of the instrument have been characterised in the lab, but for the PMTs we rely on the manufacturer's data which make no allowance for variance between units. Our practical experience with different PMT units leads us to believe such differences are significant.

The SDs given in Table 14 are typically around 6% for the middle bands. It is reasonable to expect that this figure is influenced by the modulator drift, which was the greatest during 2018AUG and the large TP on Gemini North during 2018JUN. We also noted that HD 149757 (ζ Oph—an Oe star) displayed short-term variability, and that the observation to prediction ratio for HD 203532 was typically high by 10% or more in each band. Thus, an analysis of the g' band with these observations removed was also carried out. The result is a drop in the SD by 1.5% to 4.5%. This figure is better, but is still limited by the accuracy of the literature polarisation data for the standards. All of these will have been acquired with less precise instrumentation.

5.8. Gemini north observations

Some adjustments need to be made to the correction procedure when observing on a telescope with an AltAz mount. This is because the orientation of the telescope tube and mirrors, and hence the telescope TP, relative to the sky systematically varies with parallactic angle, θ . In the ideal case, q and u for any given observation will be given by

$$q = p_{TP} \cos(2\theta - \theta_{TP}) + q_{\star} + p_i, \quad (14)$$

$$u = p_{TP} \sin(2\theta - \theta_{TP}) + u_{\star} + p_i, \quad (15)$$

where p_{TP} is the magnitude of the TP, θ_{TP} is the parallactic angle that maximises q_{TP} , and q_{\star} and u_{\star} refer to the TP-subtracted polarisation of the target in the instrument frame. The instrumental component p_i is largely eliminated by measuring each Stokes parameter at opposite PAsⁱ (e.g. 0 and 90). By making multiple observations of a star at different parallactic angles, it is possible to disentangle the star and TP, as was done with PlanetPol on the WHT (Lucas et al. 2009).

On Gemini North, the TP was far greater than on the AAT or WSU telescopes; it was also highly wavelength-dependant, being much larger at blue wavelengths. Gemini uses protected silver mirror coatings (Boccas et al. 2004; Vucina et al. 2006), whereas the other telescopes we have used have standard aluminium coatings. The silver coatings provide very high reflectance at red and infrared wavelengths but the reflectance falls off in the blue and

ⁱIt should be noted that a slight misalignment of the aperture with the instrument rotator will, since we are not re-centring at each PA, result in a slightly different area of the modulator being used and therefore a difference in p_i between angles. Any residual in this quantity gets incorporated into the TP on an equatorial telescope. On an AltAz mount, it will manifest as noise in our data if not explicitly corrected for. However, this is likely to be very small, as since adopting an observing scheme without re-centring at each PA with HIPPI-2 on the AAT, we have actually measured lower TP values, compared to those seen with HIPPI, see Figure 10. Similarly, a nonlinear response in p_i would also result in incomplete cancellation in variable conditions; something we did not see in tests made under variable cloud (Cotton et al. 2016a).

Table 15. Low-polarisation standard stars observed at Gemini North

Band		Ap	λ_{eff}	Standard observations							
Fil	PMT	(arcsec)	(nm)	A	B	C	D	E	F	G	H
425SP	B	6.4	402.9	0	0	0	0	0	4	0	0
500SP	B	6.4	443.7	0	0	0	2	0	4	0	0
g'	B	6.4	475.7	0	0	0	2	0	3	0	4
Clear	B	6.4	483.2	0	0	0	2	0	4	0	0
r'	B	6.4	605.7	0	0	0	0	0	3	0	4

Notes: The key for the letters denoting the low-polarisation standards is in Table 5.

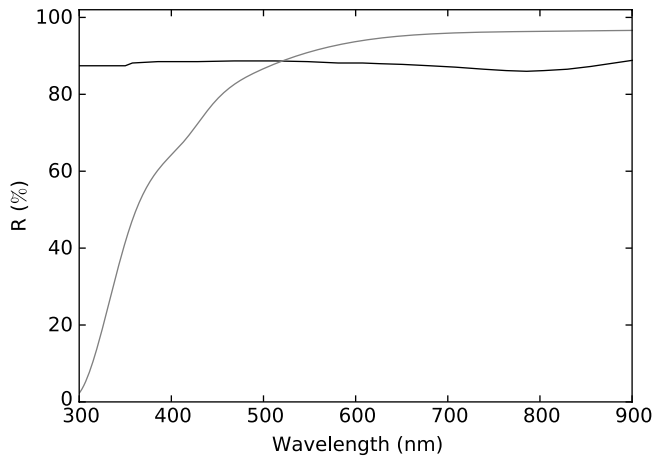


Figure 13. Reflectance of the Gemini silver-coated mirror (grey) compared to an aluminium coating (black).

UV (see Figure 13). The steep rise in TP we find occurs at the wavelengths where the mirror reflectance is declining.

The combination of high and strongly wavelength-dependent TP prevented HIPPI-2 from obtaining the same precision it does on other telescopes. While it should be theoretically possible to subtract out all of the TP with a precise wavelength solution, the scale of the TP magnifies many issues that would otherwise be insignificant. Any imprecision in the characterisation of the optical components and detectors becomes problematic, as does the smallest misalignment of the field derotator. Any imprecision in the instrument rotator alignment would also be exacerbating.

Table 15 indicates the low-polarisation standard observations made on Gemini North during the 2018JUN run. Using these observations, a first-order correction to the TP has been calculated by assuming that p_* , u_* , and p_i in equations 14 and (15) are negligible, that is, $q_{1st} = q_{TP}(\lambda)$ and $u_{1st} = u_{TP}(\lambda)$. The best-fit wavelength solution is shown in Figure 14, along with the observations. In order to achieve the best fit in this instance, a number of modifications were made to the procedure described in Section 4. The air mass, parallactic angle, and efficiency correction are calculated (at floating point precision) not just for the whole observation, but for each integration. The TP function is then calculated for each integration for each Stokes parameter in the instrumental frame, with the mean q and u determined for each observation. This step is especially necessary for observations made close to or through zenith. Additionally, Kurucz models selected for the temperature of the standards, rather than their spectral type were used since they provided a slightly better fit to the data.

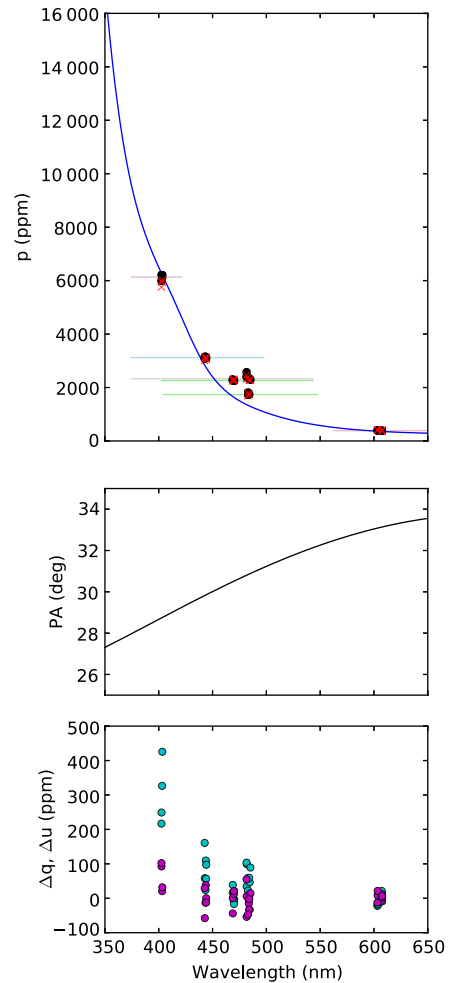


Figure 14. The first-order TP solution for Gemini North: in the top panel is the best-fit solution in p (blue line), along with the corresponding band determinations for each low-polarisation standard observation at the calculated effective wavelength (black circles), and the actual measurements (red crosses). The horizontal coloured lines are representative of the band contribution (FW10%M); the second green line has been added for the redder standard, α Ser. In the middle panel is the fitted position angle of the TP (black line). The lower panel shows the residuals in q (cyan circles) and u (magenta circles) at the effective wavelength of the observations in the instrument frame. A second-order correction is later applied to each band individually.

The PA correction is only applied after the first-order TP correction is determined and subtracted, since the TP is large enough to influence the PA determined using the high-polarisation standards observed (see Table 4).

The best-fit function in Figure 14 was arrived at through trial and error of many different functions and is based on assuming that the increase in TP is related to the fall-off in mirror reflectivity as discussed above. it has the form

$$p_{TP}(\lambda) = m(100 - R_M(\lambda))^2 + b, \tag{16}$$

where $R_M(\lambda)$ is the mirror reflectivity as a function of wavelength in percent, and m and b are constants.

The data for $R_M(\lambda)$ are taken from Feller et al. (2012) who present measurements of five mirror samples coated according to the Gemini recipe, a lab reference, one prior to cleaning in 2009, and three post cleaning in 2009, 2010, and 2011 which we used to create a grid. We linearly interpolated in this grid of spectra

Table 16. TP and instrumental corrections based on low-polarisation standard observations at Gemini North

Filter	λ_{eff} (nm)	First-order corr. ^a			Second-order corr.				Pos err. ^b	
		Obs. p	Fit p_{TP}	Fit θ_{TP}	q_{TP}	u_{TP}	q_i	u_i	ϵ_p	Prec. ^c
425SP	402.9	5925.1	6133.3	28.73	-120.4 ± 34.8	58.3 ± 33.9	261.2 ± 34.4	-30.5 ± 34.3	132.2	140.8
500SP	443.7	3084.7	3119.7	29.82	43.9 ± 23.0	-27.2 ± 23.6	114.1 ± 32.2	-3.2 ± 31.4	11.1	41.0
g'	475.7	2039.5	2042.9	30.61	18.5 ± 14.3	-8.5 ± 14.3	23.5 ± 19.7	5.1 ± 19.4	5.7	24.9
Clear	483.2	2328.7	2389.6	30.68	-1.3 ± 19.0	-36.1 ± 18.2	63.8 ± 23.0	-9.6 ± 22.4	13.2	32.2
r'	605.7	399.4	386.1	33.06	8.9 ± 4.8	4.6 ± 4.8	-10.5 ± 8.3	7.2 ± 8.2	1.1	9.7

Notes: All values of q , u , p , e , and precision are in ppm.

The q and u are given in the instrument frame and need to be rotated by 58.1° for the equatorial frame.

^a Shown are the average measured polarisations of the standards in each band, and the average fits of p_{TP} and θ_{TP} using the bandpass model. θ_{TP} represents the PA of the TP as measured for a parallactic angle of 0° as measured in the instrumental frame.

^b The positioning error ϵ_p is calculated in the same way as in Tables 9 and 12, that is, having taken account of the errors in the other quantities to the left in the table. In addition to the low-polarisation standards, repeat observations of two other stars thought to have low levels of constant polarisation were also considered.

^c The final precision estimate considers all the stated errors as the square root of the sum of the means squared.

based on two parameters, the age a and condition c (where $c = 0$ after cleaning and $c = 1$ before cleaning). The values of the parameters $a = 2009.0$ and $c = 0.2631$ as well as $m = 4.9474$ and $b = 175.9$ were determined by fitting the standard star observations using Python's CURVE_FIT routine.

In addition, we also simultaneously fit a polynomial to describe the TP position angle as a function of wavelength

$$PA_{ip}(\lambda) = \frac{\alpha}{\lambda} + \beta + \gamma\lambda + \delta\lambda^2 + \epsilon\lambda^3, \quad (17)$$

where λ is given in nanometers and the coefficients denoted by the greek letters are fit to be -728.96 , 4696.4 , -18.0912 , 0.11829934 , and $-7.68615733 \times 10^{-5}$, respectively.

The resultant function is shown in the middle panel of Figure 14.

As shown in Figure 14, after the subtraction of $p_{TP}(\lambda)$, there are still significant residuals in the low-polarisation standard measurements, where the disagreement is largest in the two short-pass bands (and appears more down to the fit PA than the fit p). A second-order correction has been applied to each band individually. This correction takes the form

$$q_{2nd} = q_{TP} + q_i, \quad (18)$$

$$u_{2nd} = u_{TP} + u_i, \quad (19)$$

where the q_{TP} and u_{TP} are functions of the parallactic angle, as in equation 14 and (15). By fitting these equations using the PYTHON package SCIPY's CURVE_FIT routine (Jones et al. 2001), an error in each term is obtained which allows the precision of the instrument on the telescope to be quantified. The corrections and associated errors are shown in Table 16. As these values dwarfed the expected values of q_* and u_* for the standards, attempts to retrieve them were abandoned.

6. Conclusions

We have built and tested a new versatile and compact high-precision polarimeter HIPPI-2. The instrument is based on a FLC modulator as used in its predecessor HIPPI. HIPPI-2 is constructed largely by 3D printing. It weighs about 4 kg and requires a single compact electronics box weighing 1.3 kg containing its data acquisition electronics and computer. The new instrument has been tested on three telescopes, the 60-cm Ritchey-Chretien telescope at WSU's Penrith Observatory, the 3.9-m AAT, and the 8.1-m Gemini North Telescope.

On the AAT, HIPPI-2 achieves a precision as measured from repeat observations of low-polarisation stars in the g' band of better than 3.5 ppm and probably around 2–3 ppm. Precision is somewhat better at red wavelengths and poorer at blue wavelengths. On the WSU telescope, the precision in the g' band is better than 11 ppm and probably around 7–8 ppm. We believe the limit on the precision is set by the accuracy with which stars can be kept centred on the instrument axis, and thus the better precision with the AAT reflects its more accurate tracking and guiding.

The TP measured at the WSU telescope ranged from 10 to 40 ppm. The TP at the AAT ranged from 10 to 300 ppm with the highest values occurring with an $f/15$ secondary that had not been realuminised for 20 yr. When this mirror was recoated, much lower values (around 10 ppm in most bands) were obtained. These telescopes use standard aluminium mirror coatings.

On the Gemini North telescope, which uses protected silver mirror coatings, we found much higher and strongly wavelength-dependent TP, increasing from ~ 400 ppm in the r' band to ~ 6000 ppm at 400 nm. While we have developed a model to correct for the high TP, the strong wavelength dependence introduces uncertainties that limit the precision to ~ 10 ppm at the r' band, ~ 25 ppm at the g' band, and much worse at bluer bands.

On the AAT, HIPPI-2 provides improved precision, throughput and observing efficiency compared with its predecessor, HIPPI, which has already proven to be a very scientifically productive instrument. The compact size allows HIPPI-2 to be easily adapted to a range of telescopes including relatively small telescopes such as the 60-cm WSU telescope.

Acknowledgements. We thank the former Director of the Australian Astronomical Observatory, Prof. Warrick Couch, and the current Director of Siding Spring Observatory, A/Prof. Chris Lidman for their support of the HIPPI-2 project on the AAT. We thank Prof. Miroslav Filipovic for providing access to the Penrith Observatory. Funding for the construction of HIPPI-2 was provided by UNSW through the Science Faculty Research Grants Program. Nicholas Borsato, Dag Evensberget, Behrooz Karamiucham, Fiona Lewis, Shannon Melrose, and Jinglin Zhao assisted with observations at the AAT. Based on observations under programme GN-2018A-DD-108, obtained at the Gemini Observatory, which is operated by the Association of Universities for Research in Astronomy, Inc., under a cooperative agreement with the NSF on behalf of the Gemini partnership: the National Science Foundation (United States), the National Research Council (Canada), CONICYT (Chile), Ministerio de Ciencia, Tecnología e Innovación Productiva (Argentina), and Ministério da Ciência, Tecnologia e Inovação (Brazil). This research has made use of the SIMBAD database, operated at CDS, Strasbourg, France.

References

- Astropy Collaboration et al. 2013, *A&A*, **558**, A33
- Astropy Collaboration et al. 2018, *AJ*, **156**, 123
- Bagnulo, S., et al. 2017, *A&A*, **608**, A146
- Bailey, J., Cotton, D. V., & Kedziora-Chudczer, L. 2017, *MNRAS*, **465**, 1601
- Bailey, J., Cotton, D. V., Kedziora-Chudczer, L., De Horta, A., & Maybour, D. 2019, *NatAs*, **3**, 636
- Bailey, J., & Kedziora-Chudczer, L. 2012, *MNRAS*, **419**, 1913
- Bailey, J., Kedziora-Chudczer, L., Cotton, D. V., Bott, K., Hough, J. H., & Lucas, P. W. 2015, *MNRAS*, **449**, 3064
- Bailey, J., Lucas, P. W., & Hough, J. H. 2010, *MNRAS*, **405**, 2570
- Bastien, P., Drissen, L., Menard, F., Moffat, A. F. J., Robert, C., & St-Louis, N. 1988, *AJ*, **95**, 900
- Boccas, M., Vucina, T., Araya, C., Vera, E., & Ahhee, C. 2004, in *Proc. SPIE*, Vol. 5494, *Optical Fabrication, Metrology, and Material Advancements for Telescopes*, ed. E. Atad-Ettedgui & P. Dierickx, 239–253, doi:10.1117/12.548809
- Bott, K., Bailey, J., Kedziora-Chudczer, L., Cotton, D. V., Lucas, P. W., Marshall, J. P., & Hough, J. H. 2016, *MNRAS*, **459**, L109
- Bott, K., Bailey, J., Cotton, D. V., Kedziora-Chudczer, L., Marshall, J. P., & Meadows, V. S. 2018, *AJ*, **156**, 293
- Cardelli, J. A., Clayton, G. C., & Mathis, J. S. 1989, *ApJ*, **345**, 245
- Castelli, F., & Kurucz, R. L. 2004, *ArXiv Astrophysics e-prints*, (arXiv:astro-ph/0405087)
- Cotton, D. V., Bailey, J., Kedziora-Chudczer, L., Bott, K., Lucas, P. W., Hough, J. H., & Marshall, J. P. 2016a, *MNRAS*, **455**, 1607
- Cotton, D. V., Bailey, J., Kedziora-Chudczer, L., Bott, K., Lucas, P. W., Hough, J. H., & Marshall, J. P. 2016b, *MNRAS*, **460**, 18
- Cotton, D. V., Bailey, J., Howarth, I. D., Bott, K., Kedziora-Chudczer, L., Lucas, P. W., & Hough, J. H. 2017a, *NatAs*, **1**, 690
- Cotton, D. V., Marshall, J. P., Bailey, J., Kedziora-Chudczer, L., Bott, K., Marsden, S. C., & Carter, B. D. 2017b, *MNRAS*, **467**, 873
- Cotton, D. V., et al. 2019a, *MNRAS*, **483**, 1574
- Cotton, D. V., et al. 2019b, *MNRAS*, **483**, 3636
- Feller, A., Krishnappa, N., Pleier, O., Hirzberger, J., Jobst, P. J., & Schürmann, M. 2012, in *Modern Technologies in Space- and Ground-based Telescopes and Instrumentation II*, 84503U, doi:10.1117/12.927080
- Ginsburg, A., et al. 2019, *AJ*, **157**, 98
- Gisler, D., Feller, A., & Gandorfer, A. M. 2003, in *Proc. SPIE*, Vol. 4843, *Polarimetry in Astronomy*, ed. S. Fineschi, 45–54, doi:10.1117/12.458835
- Guthrie, B. N. G. 1987, *QJRAS*, **28**, 289
- Horton, A., et al. 2012, in *Proc. SPIE*, 84463A (arXiv:1301.0670), doi:10.1117/12.924945
- Hough, J. H., Lucas, P. W., Bailey, J. A., Tamura, M., Hirst, E., Harrison, D., & Bartholomew-Biggs, M. 2006, *PASP*, **118**, 1302
- Hsu, J. C., & Breger, M. 1982, *ApJ*, **262**, 732
- Hunter, J. D. 2007, *Computing in Science & Engineering*, **9**, 90
- Jones, E., Oliphant, T., & Peterson, P., et al. 2001, *SciPy: Open source scientific tools for Python*, <http://www.scipy.org/>
- Kemp, J. C., & Barbour, M. S. 1981, *PASP*, **93**, 521
- Lucas, P. W., Hough, J. H., Bailey, J. A., Tamura, M., Hirst, E., & Harrison, D. 2009, *MNRAS*, **393**, 229
- Marshall, J. P., et al. 2016, *ApJ*, **825**, 124
- Martin, P. G., Clayton, G. C., Wolff, M. J. 1999, *ApJ*, **510**, 905
- McDavid, D. 2000, *AJ*, **119**, 352
- Morris, B. M., et al. 2018, *AJ*, **155**, 128
- Nakamura, K., Hamana, Y., Ishigami, Y., & Matsui, T. 2010, *Nuclear Instruments and Methods in Physics Research A*, **623**, 276
- Oliphant, T. E. 2006, *A guide to NumPy*. Vol. 1 (USA: Trelgol Publishing)
- Patriarchi, P., Morbidelli, L., Perinotto, M., & Barbaro, G. 2001, *A&A*, **372**, 644
- Pirola, V., Berdyugin, A., & Berdyugina, S., 2014, in *Ground-based and Airborne Instrumentation for Astronomy V*, 91478L, doi:10.1117/12.2055923
- Serkowski, K. 1974, in *IAU Colloq. 23: Planets, Stars, and Nebulae: Studied with Photopolarimetry*, ed. T. Gehrels, 135
- Serkowski, K., Mathewson, D. S., & Ford, V. L. 1975, *ApJ*, **196**, 261
- Vucina, T., Boccas, M., Araya, C., & Ahhee, C. 2006, in *Society of Photo-Optical Instrumentation Engineers (SPIE) Conference Series*, 62730W, doi:10.1117/12.670866
- Wiktorowicz, S. J., & Matthews, K. 2008, *PASP*, **120**, 1282
- Wiktorowicz, S. J., & Nofi, L. A. 2015, *ApJ*, **800**, L1
- Wilking, B. A., Lebofsky, M. J., Martin, P. G., Rieke, G. H., & Kemp, J. C. 1980, *ApJ*, **235**, 905
- Wilking, B. A., Lebofsky, M. J., Rieke, G. H., 1982, *AJ*, **87**, 695

Appendix A. Modulation efficiency at high and low polarisation

As mentioned in Section 4.2.1, the modulation efficiency measured for the instrument is different when illuminated with 100% polarised light in the laboratory and when observing astronomical sources with low polarisations. The difference arises because of the way the polarisation alters the average intensity of the two beams when the modulator departs from the ideal half-wave retardance.

The instrument is essentially a retarder (the FLC modulator) followed by a polariser (the Wollaston prism). The Mueller matrix for a retarder is (Bailey et al. 2015):

$$\begin{bmatrix} 1 & 0 & 0 & 0 \\ 0 & C^2 + S^2 \cos \delta & SC(1 - \cos \delta) & -S \sin \delta \\ 0 & SC(1 - \cos \delta) & S^2 + C^2 \cos \delta & C \sin \delta \\ 0 & S \sin \delta & -C \sin \delta & \cos \delta \end{bmatrix}, \quad (\text{A.1})$$

where $C = \cos 2\phi$, $S = \sin 2\phi$, δ is the retardance, and ϕ the angle to the fast axis of the retarder. For a half-wave plate, the retardance is π radians.

The Mueller matrix for the polariser is

$$1/2 \begin{bmatrix} 1 & c & s & 0 \\ c & c^2 & sc & 0 \\ s & cs & s^2 & 0 \\ 0 & 0 & 0 & 0 \end{bmatrix}, \quad (\text{A.2})$$

where $c = \cos 2\theta$, $s = \sin 2\theta$, θ is the angle of the polariser axis to that defined for the incoming beam.

Consider the effect of these optical elements on a polarised input beam with Stokes vector $\{1, q, 0, 0\}$. Multiplying by the top two rows of the retarder matrix gives

$$I = 1, \quad (\text{A.3})$$

$$Q = (C^2 + S^2 \cos \delta)q, \quad (\text{A.4})$$

for the I and Q Stokes parameters after the retarder. If the two orientations of the fast axis of the modulator for the two modulation states are $\phi = 0^\circ$ ($C = 1$, $S = 0$) and $\phi = 45^\circ$ ($C = 0$, $S = 1$), then equation A.4 becomes

$$Q_1 = q, \quad (\text{A.5})$$

$$Q_2 = q \cos \delta, \quad (\text{A.6})$$

for the two modulation states and we can then multiply by the top row of the polariser matrix to get the output intensity in each state (assuming $\theta = 0$ and hence $c = 1$):

$$I_1 = 0.5(1 + q), \quad (\text{A.7})$$

$$I_2 = 0.5(1 + q \cos \delta). \quad (\text{A.8})$$

The intensities in the second Wollaston beam for which we can assume $\theta = 90^\circ$ and hence $c = -1$ are the same equations with a minus sign replacing the plus sign. The modulation that we measure is given by:

$$M_A = \frac{I_1 - I_2}{I_1 + I_2} = \frac{q(1 - \cos \delta)}{2 + q + q \cos \delta}, \quad (\text{A.9})$$

and the equivalent for the second Wollaston beam is

$$M_B = \frac{I_1 - I_2}{I_1 + I_2} = \frac{-q(1 - \cos \delta)}{2 - q - q \cos \delta}. \quad (\text{A.10})$$

The minus sign here meaning that the modulation in the two Wollaston beams are of opposite signs. The modulation efficiency is the modulation divided by the input polarisation (i.e. M_A/q and M_B/q).

We can now consider several special cases of the general formulae in equations (A.9) and (A.10). If the modulator is a half-wave retarder, then $\cos \delta = -1$ and therefore,

$$M_A/q = 1, \quad (\text{A.11})$$

$$M_B/q = -1. \quad (\text{A.12})$$

This is the ideal case giving 100% modulation efficiency.

If q is very much less than one (i.e. low polarisation), then we can ignore the q and $q \cos \delta$ terms in the denominator and we get

$$M_A/q = \frac{1 - \cos \delta}{2}, \quad (\text{A.13})$$

$$M_B/q = -\frac{1 - \cos \delta}{2}, \quad (\text{A.14})$$

which is the form used in equation 10.

If $q = 1$ (i.e. 100% input polarisation as in our laboratory calibration), then we get

$$M_A/q = \frac{1 - \cos \delta}{3 + \cos \delta}, \quad (\text{A.15})$$

$$M_B/q = -\frac{1 - \cos \delta}{1 - \cos \delta} = -1. \quad (\text{A.16})$$

In this case, the modulation efficiencies for the two beams have different magnitudes as well as opposite signs. Averaging the magnitude of these two gives the expression used in equation 8.

In other cases where the polarisation is large, equations (A.9) and (A.10) must be used.